Planck 2013 results. XXXI. Consistency of the *Planck* data

Planck Collaboration: P. A. R. Ade[77], M. Arnaud[66], M. Ashdown[63,6], J. Aumont[53], C. Baccigalupi[76], A. J. Banday[83,9],
R. B. Barreiro[60], E. Battaner[84,85], K. Benabed[54,82], A. Benoit-Lévy[21,54,82], J.-P. Bernard[83,9], M. Bersanelli[30,44], P. Bielewicz[83,9,76],
J. R. Bond[8], J. Borrill[12,79], F. R. Bouchet[54,82], C. Burigana[43,28], J.-F. Cardoso[67,1,54], A. Catalano[68,65], A. Challinor[56,63,11],
A. Chamballu[66,13,53], H. C. Chiang[24,7], P. R. Christensen[73,33], D. L. Clements[50], S. Colombi[54,82], L. P. L. Colombo[20,61],
F. Couchot[64], A. Coulais[65], B. P. Crill[61,74], A. Curto[6,60], F. Cuttaia[43], L. Danese[76], R. D. Davies[62], R. J. Davis[62], P. de Bernardis[29],
A. de Rosa[43], G. de Zotti[40,76], J. Delabrouille[1], F.-X. Désert[48], C. Dickinson[62], J. M. Diego[60], H. Dole[53,52], S. Donzelli[44],
O. Doré[61,10], M. Douspis[53], X. Dupac[35], T. A. Enßlin[70], H. K. Eriksen[57], F. Finelli[43,45], O. Forni[83,9], M. Frailis[42], A. A. Fraisse[24],
E. Franceschi[43], S. Galeotta[42], K. Ganga[1], M. Giard[83,9], J. González-Nuevo[60,76], K. M. Górski[61,86], S. Gratton[63,56],
A. Gregorio[31,42,47], A. Gruppuso[43], J. E. Gudmundsson[24], F. K. Hansen[57], D. Hanson[71,61,8], D. L. Harrison[56,63],
S. Henrot-Versillé[64], D. Herranz[60], S. R. Hildebrandt[61], E. Hivon[54,82], M. Hobson[6], W. A. Holmes[61], A. Hornstrup[14], W. Hovest[70],
K. M. Huffenberger[22], A. H. Jaffe[50], T. R. Jaffe[83,9], W. C. Jones[24], E. Keihänen[23], R. Keskitalo[18,12], J. Knoche[70], M. Kunz[15,53,3],
H. Kurki-Suonio[23,39], G. Lagache[53], A. Lähteenmäki[2,39], J.-M. Lamarre[65], A. Lasenby[6,63], C. R. Lawrence[61,*], R. Leonardi[35],
J. León-Tavares[58,37,2], J. Lesgourgues[81,75], M. Liguori[27], P. B. Lilje[57], M. Linden-Vørnle[14], M. López-Caniego[60], P. M. Lubin[25],
J. F. Macías-Pérez[68], D. Maino[30,44], N. Mandolesi[43,5,28], M. Maris[42], P. G. Martin[8], E. Martínez-González[60], S. Masi[29],
S. Matarrese[27], P. Mazzotta[32], P. R. Meinhold[25], A. Melchiorri[29,46], L. Mendes[35], A. Mennella[30,44], M. Migliaccio[56,63],
S. Mitra[49,61], M.-A. Miville-Deschênes[53,8], A. Moneti[54], L. Montier[83,9], G. Morgante[43], D. Mortlock[50], A. Moss[78], D. Munshi[77],
J. A. Murphy[72], P. Naselsky[73,33], F. Nati[29], P. Natoli[28,4,43], H. U. Nørgaard-Nielsen[14], F. Noviello[62], D. Novikov[50], I. Novikov[73],
C. A. Oxborrow[14], L. Pagano[29,46], F. Pajot[53], D. Paoletti[43,45], B. Partridge[38], F. Pasian[42], G. Patanchon[1], D. Pearson[61],
T. J. Pearson[10,51], O. Perdereau[64], F. Perrotta[76], F. Piacentini[29], M. Piat[1], E. Pierpaoli[20], D. Pietrobon[61], S. Plaszczynski[64],
E. Pointecouteau[83,9], G. Polenta[4,41], N. Ponthieu[53,48], L. Popa[55], G. W. Pratt[66], S. Prunet[54,82], J.-L. Puget[53], J. P. Rachen[17,70],
M. Reinecke[70], M. Remazeilles[62,53,1], C. Renault[68], S. Ricciardi[43], I. Ristorcelli[83,9], G. Rocha[61,10], G. Roudier[1,65,61],
J. A. Rubiño-Martín[59,34], B. Rusholme[51], M. Sandri[43], D. Scott[19], V. Stolyarov[6,63,80], R. Sudiwala[77], D. Sutton[56,63],
A.-S. Suur-Uski[23,39], J.-F. Sygnet[54], J. A. Tauber[36], L. Terenzi[43], L. Toffolatti[16,60], M. Tomasi[30,44], M. Tristram[64], M. Tucci[15,64],
L. Valenziano[43], J. Valiviita[23,39], B. Van Tent[69], P. Vielva[60], F. Villa[43], L. A. Wade[61], B. D. Wandelt[54,82,26], I. K. Wehus[61,10],
S. D. M. White[70], D. Yvon[13], A. Zacchei[42], and A. Zonca[25]

(Affiliations can be found after the references)

ABSTRACT

The *Planck* design and scanning strategy provide many levels of redundancy that can be exploited to provide tests of internal consistency. One of the most important is the comparison of the 70 GHz (amplifier) and 100 GHz (bolometer) channels. Based on different instrument technologies, with feeds located differently in the focal plane, analysed independently by different teams using different software, and near the minimum of diffuse foreground emission, these channels are in effect two different experiments. The 143 GHz channel has the lowest noise level on *Planck*, and is near the minimum of unresolved foreground emission. In this paper, we analyse the level of consistency achieved in the 2013 *Planck* data. We concentrate on comparisons between the 70, 100, and 143 GHz channel maps and power spectra, particularly over the angular scales of the first and second acoustic peaks, on maps masked for diffuse Galactic emission and for strong unresolved sources. Difference maps covering angular scales from 8° to 15′ are consistent with noise, and show no evidence of cosmic microwave background structure. Including small but important corrections for unresolved-source residuals, we demonstrate agreement (measured by deviation of the ratio from unity) between 70 and 100 GHz power spectra averaged over $70 \leq \ell \leq 390$ at the 0.8% level, and agreement between 143 and 100 GHz power spectra of 0.4% over the same ℓ range. These values are within and consistent with the overall uncertainties in calibration given in the *Planck* 2013 results. We also present results based on the 2013 likelihood analysis showing consistency at the 0.35% between the 100, 143, and 217 GHz power spectra. We analyse calibration procedures and beams to determine what fraction of these differences can be accounted for by known approximations or systematic errors that could be controlled even better in the future, reducing uncertainties still further. Several possible small improvements are described. Subsequent analysis of the beams quantifies the importance of asymmetry in the near sidelobes, which was not fully accounted for initially, affecting the 70/100 ratio. Correcting for this, the 70, 100, and 143 GHz power spectra agree to 0.4% over the first two acoustic peaks. The likelihood analysis that produced the 2013 cosmological parameters incorporated uncertainties larger than this. We show explicitly that correction of the missing near sidelobe power in the HFI channels would result in shifts in the posterior distributions of parameters of less than 0.3σ except for A_s, the amplitude of the primordial curvature perturbations at $0.05\,\mathrm{Mpc}^{-1}$, which changes by about 1σ. We extend these comparisons to include the sky maps from the complete nine-year mission of the *Wilkinson* Microwave Anisotropy Probe (WMAP), and find a roughly 2% difference between the *Planck* and WMAP power spectra in the region of the first acoustic peak.

Key words. cosmology: observations – cosmic microwave background – instrumentation: detectors

* Corresponding author: C. R. Lawrence, e-mail: `charles.lawrence@jpl.nasa.gov`

1. Introduction

This paper, one of a set associated with the 2013 release of data from the *Planck*[1] mission (Planck Collaboration I 2014), describes aspects of the internal consistency of the *Planck* data in the 2013 release not addressed in the other papers. The *Planck* design and scanning strategy provide many levels of redundancy, which can be exploited to provide tests of consistency (Planck Collaboration I 2014), most of which are carried out routinely in the *Planck* data processing pipelines (Planck Collaboration II 2014; Planck Collaboration VI 2014; Planck Collaboration XV 2014; Planck Collaboration XVI 2014). One of the most important consistency tests for *Planck* is the comparison of the LFI and HFI channels, and indeed this was a key feature of its original experimental concept. Based on different instrument technologies, with feeds located differently in the focal plane, and analysed independently by different teams, these two instruments provide a powerful mutual assessment and test of systematic errors. This paper focuses on comparison of the LFI and HFI channels closest in frequency to each other and to the diffuse foreground minimum, namely the 70 GHz (LFI) and 100 GHz (HFI) channels[2], together with the 143 GHz HFI channel, which has the greatest sensitivity to the cosmic microwave background (CMB) of all the *Planck* channels.

Quantitative comparisons involving different frequencies must take into account the effects of frequency-dependent foregrounds, both diffuse and unresolved. *Planck* processing for the 2013 results proceeds along two main lines, depending on the scientific purpose. For non-Gaussianity and higher-order statistics, and for the $\ell < 50$ likelihood, diffuse foregrounds are separated at map level (Planck Collaboration XII 2014). Only the strongest unresolved sources, however, can be identified and masked from the maps, and the effects of residual unresolved foregrounds must be dealt with statistically. They therefore require corrections later in processing (e.g., Planck Collaboration XXIII 2014; Planck Collaboration XXIV 2014). For power spectra, the $\ell \geq 50$ likelihood, and parameters, both diffuse and unresolved source residuals are handled in the power spectra with a combination of masking and fitting of a parametric foreground model (Planck Collaboration XVI 2014).

In this paper, we compare *Planck* channels for consistency in two different ways. First, in Sects. 2 and 3, we compare frequency maps from the *Planck* 2013 data release – available from the *Planck* Legacy Archive (PLA)[3] and referred to hereafter as PLA maps – and power spectra calculated from them, looking first at the effects of noise and foregrounds (both diffuse and unresolved), and then, in Sect. 4, at calibration and beam effects. This comparison based on publicly released maps ties effects in the data directly to characteristics of the instruments and their determination. This examination has provided important insights into our calibration and beam determination procedures even since the 2013 results were first released publicly in March 2013, confirming the validity of the 2013 cosmological results, resolving some issues that had been contributing to the uncertainties,

and suggesting future improvements that will reduce uncertainties further.

Second, in Sect. 5, we compare power spectra again, this time from the "detector set" data at 100, 143, and 217 GHz (see Table 1 in Planck Collaboration XV 2014) used in the likelihood analysis described in Planck Collaboration XV (2014), but extending that analysis to include 70 GHz as well. These detector-set/likelihood comparisons give a measure of the agreement between frequencies in the data used to generate the *Planck* 2013 cosmological parameter results in Planck Collaboration XVI (2014). Taking into account differences in the data and processing, the same level of consistency is seen as in the comparison based on PLA frequency maps in Sect. 3. We then show that the small changes in beam window functions discussed in Sect. 4 have no significant effect on the 2013 parameter results other than the overall amplitude of the primordial curvature perturbations at $0.05\,\mathrm{Mpc}^{-1}$, $A_{\rm s}$.

After having established consistency within the *Planck* data, specifically agreement between 70, 100, and 143 GHz over the first acoustic peak to better than 0.5% in the power spectrum, in Sect. 6 we compare *Planck* with WMAP, specifically the WMAP9 release[4]. The absolute calibration of the *Planck* 2013 results is based on the "solar dipole" (i.e., the motion of the Solar System barycentre with respect to the CMB) determined by WMAP7 (Hinshaw et al. 2009), whose uncertainty leads to a calibration error of 0.25% (Planck Collaboration V 2014). For the *Planck* channels considered in this paper, the overall calibration uncertainty is 0.6% in the 70 GHz maps and 0.5% in the 100 and 143 GHz maps (1.2% and 1.0%, respectively, in the power spectra; Planck Collaboration I 2014, Table 6). When comparing *Planck* and WMAP calibrated maps, however, one should remove from these uncertainties in the *Planck* maps the 0.25% contribution from the WMAP dipole, since it was the reference calibrator for both LFI and HFI. In the planned 2014 release, the *Planck* absolute calibration will be based on the "orbital dipole" (i.e., the modulation of the solar dipole due to the Earth's orbital motion around the Sun), bypassing uncertainties in the solar dipole.

Throughout this paper we refer to frequency bands by their nominal designations of 30, 44, 70, 100, 143, 217, 353, 545, and 857 GHz for *Planck* and 23, 33, 41, 61, and 94 GHz for WMAP; however, we take bandpasses into account in all calculations. The actual weighted central frequencies determined by convolution of the bandpass response with a CMB spectrum are 28.4, 44.1, 70.4, 100.0, 143.0, 217.0, 353.0, 545.0, and 857.0 GHz for *Planck*, and 22.8, 33.2, 41.0, 61.4, and 94.0 GHz for WMAP. These correspond to the effective frequencies for CMB emission. For emission with different spectra, the effective frequency is slightly shifted.

The maps discussed in this paper are structured according to the HEALPix[5] scheme (Górski et al. 2005) displayed in Mollweide projections in Galactic coordinates.

2. Comparison of frequency maps

The *Planck* 2013 data release includes maps based on 15.5 months of data, as well as maps of subsets of the data that enable tests of data quality and systematic errors. Examples include (see Planck Collaboration I 2014 for complete descriptions) single survey maps and half-ring difference maps, made

---

[2] The frequency at which extragalactic foregrounds are at a minimum level depends on angular scale, shifting from around 65 GHz at low ℓ to 143 GHz at $\ell \approx 200$.

[3] http://archives.esac.esa.int/pla2

[4] Available from the LAMBDA site: http://lambda.gsfc.nasa.gov

[5] See http://healpix.jpl.nasa.gov
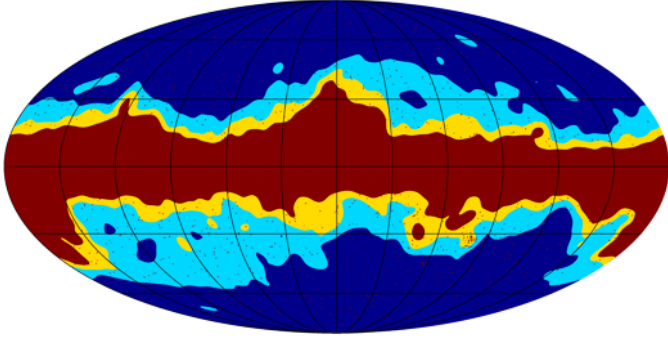
Fig. 1. Sky masks used for spectral analysis of the *Planck* 70, 100, and 143 GHz maps. The light light blue, yellow, and red masks leave observable sky fractions f_{sky} of 39.7%, 59.6%, and 69.4%, respectively, and are named GAL040, GAL060, and GAL070 in the PLA. These masks are extended by exclusion of unresolved sources in the PCCS 70, 100, and 143 GHz source lists above the 5σ flux density cuts.

by splitting the data from each pointing period of the satellite into halves, making separate sky maps from the two halves, and taking the difference of the two maps. Half-ring maps are particularly useful in characterizing the noise, and also enable signal estimation based on cross-spectra, with significant noise reduction compared to auto-spectra.

The 100 and 143 GHz maps are released at `HEALPix` resolution $N_{side} = 2048$, with $N_{pix} = 12 \times N_{side}^2 \approx 5 \times 10^7$ pixels of approximately $1\!'.7$. Although the LFI maps are generally released at $N_{side} = 1024$, the 70 GHz maps are also released at $N_{side} = 2048$. All mapmaking steps except map binning at the given pixel resolution are the same for the two resolutions. In this paper we use the 70 GHz maps made at $N_{side} = 2048$ for comparison with the 100 and 143 GHz sky maps.

2.1. Sky masks

Comparison of maps at different frequencies over the full sky is quite revealing of foregrounds, as will be seen. For most purposes in this paper we need to mask regions of strong foreground emission. We do this using the publicly-released[6] Galactic masks GAL040, GAL060, and GAL070, shown in Fig. 1. These leave unmasked $f_{sky} = 39.7\%$, 59.6%, and 69.4% of the full sky. We mask unresolved ("point") sources detected above 5σ in the 70, 100, and 143 GHz channels, as described in the *Planck* Catalogue of Compact Sources (PCCS; Planck Collaboration XXVIII 2014). The point source masks are circular holes centred on detected sources with diameter 2.25 times the FWHM beamsize of the frequency channel in question. The masks are unapodized, as the effect of apodization on large angular scales is primarily to improve the accuracy of covariance matrices.

2.2. Monopole/dipole removal

The *Planck* data have an undetermined absolute zero level, and the *Planck* maps contain low-amplitude offsets generated in the process of mapmaking, as well as small residual dipoles that remain after removal of the kinematic dipole anisotropy. We remove the $\ell = 0$ and $\ell = 1$ modes from the maps using χ^2-minimization and the GAL040 mask, extended where applicable to a constant latitude of $\pm45°$. Diffuse Galactic emission at

---

[6] Available from the *Planck* Legacy Archive: http://archives.esac.esa.int/pla2

both low and high frequencies is still present even at high latitude, so this first step can leave residual offsets that become visible at the few microkelvin level in the difference maps smoothed to 8° shown in Appendix A. In those cases, a small offset adjustment, typically no more than a few microkelvin, is made to keep the mean value very close to zero in patches of sky visually clear of foregrounds.

2.3. Comparisons

Figure 2 shows the monopole- and dipole-removed maps at 70, 100, and 143 GHz, along with the corresponding half-ring difference maps. Figure 3 shows the difference maps between these three frequencies. The strong frequency-dependence of foregrounds is obvious. Equally obvious, and the essential point of the comparison, is the nearly complete nulling of the CMB anisotropies. This shows that these three channels on *Planck* are measuring the same CMB sky.

For a quantitative comparison, we calculate root mean square (rms) values of unmasked regions of the frequency and difference maps shown in Figs. 2 and 3, for the three masks shown in Fig. 1. To avoid spurious values caused on small scales by the differing angular resolution of the three frequencies, and on large scales by diffuse foregrounds, we first smooth the maps to a common resolution of $15'$. We then smooth them further to 8° resolution, and subtract the 8° maps from the $15'$ maps. This leaves maps that can be directly compared for structure on angular scales from 8° to $15'$. We calculate rms values for half-ring sum ("Freq.") and half-ring difference ("Diff.") maps at 70, 100, and 143 GHz, and for the frequency-difference maps 70 GHz−100 GHz, 70 GHz−143 GHz, and 100 GHz−143 GHz. The rms values are given in Table 1. The maps are shown in Fig. A.1. Histograms of the frequency maps and difference maps are shown in Fig. 4.

Except for obvious foreground structures and noise, the difference maps lie close to zero, showing the excellent agreement between the three *Planck* frequencies for the CMB anisotropies.

The map comparisons give a comprehensive view of consistency between 70, 100, and 143 GHz, but the two-dimensional nature of the comparisons makes it somewhat difficult to grasp the key similarities. To make this easier, we turn now to comparisons at the power spectrum level.

3. Comparison of power spectra from 2013 results frequency maps

Power spectra of the unmasked regions of the maps are estimated as follows.

- Starting from half-ring maps (Sect. 5.1 of Planck Collaboration I 2014), cross-spectra are computed on the masked, incomplete sky using the `HEALPix` routine `anafast` with $\ell = 0$, 1 removal. These are so-called "pseudo-spectra".
- The `MASTER` spectral coupling kernel (Hivon et al. 2002), which describes spectral mode coupling on an incomplete sky, is calculated based on the mask used. The pseudo-spectra from the previous step are converted to 4π-equivalent amplitude using the inverse of the `MASTER` kernel.
- Beam and pixel smoothing effects are removed from the spectra by dividing out the appropriate beam and pixel window functions. Beam response functions in ℓ space are required. We use the effective beam window functions derived using `FEBeCoP` (Mitra et al. 2011).
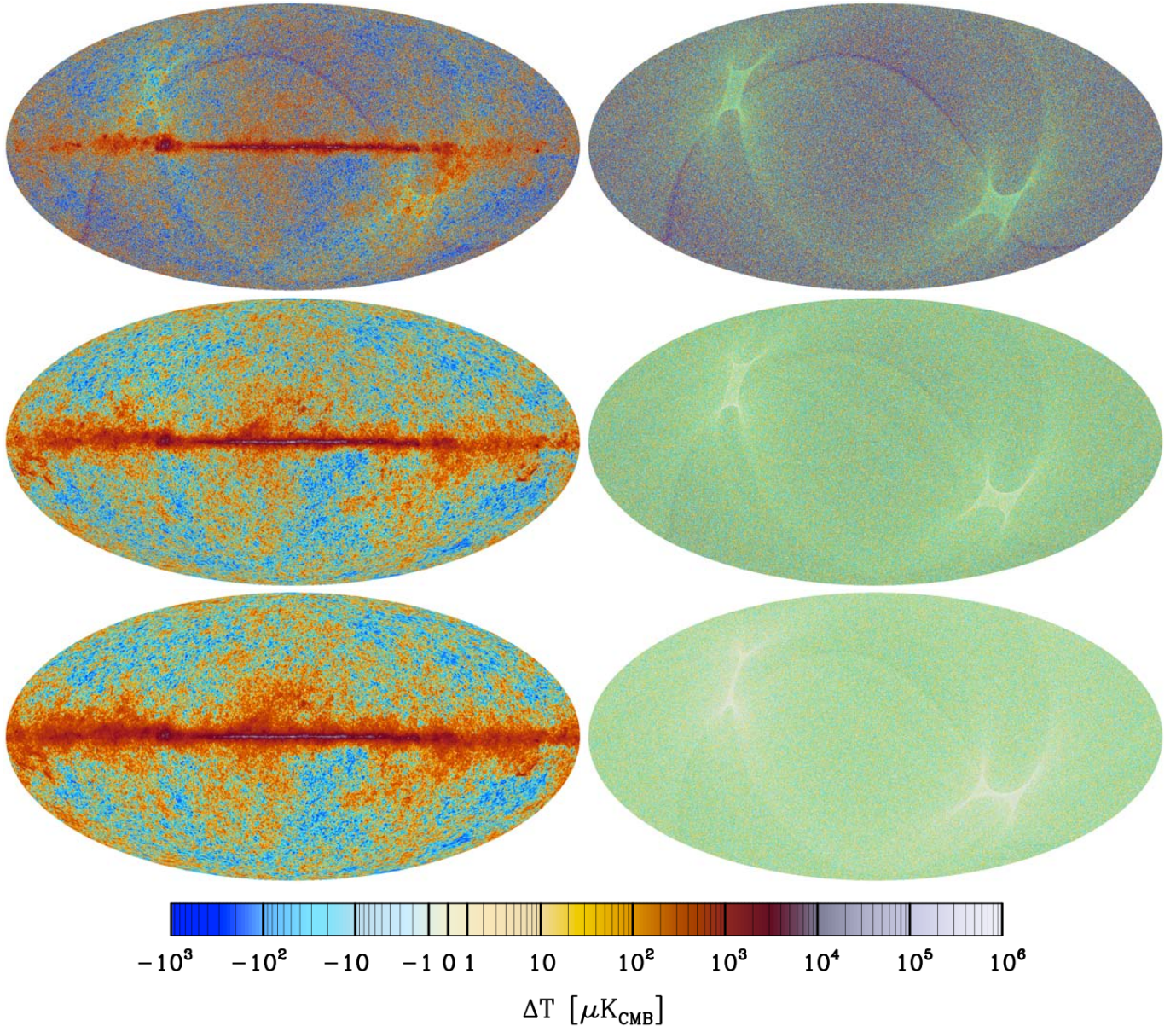
Fig. 2. Sky maps used in the analysis of *Planck* data consistency. *Top row*: 70 GHz. *Middle row*: 100 GHz. *Bottom row*: 143 GHz. *Left column*: signal maps. *Right column*: noise maps derived from half-ring differences. All maps are N_{side} = 2048. These are the publicly-released maps corrected for monopole and dipole terms as described in the text. The impression of overall colour differences between the maps is due to the interaction between noise, the colour scale, and display resolution. For example, the larger positive and negative swings between pixels in the 70 GHz noise map pick up darker reds and blues farther from zero. Smaller swings around zero in the 100 and 143 GHz noise maps result in pastel yellows and blues in adjacent pixels, which when displayed at less than full-pixel resolution give an overall impression of green, a colour not used in the colour bar.

3.1. Spectral analysis of signals and noise

Figure 5 shows the signal (half-ring map cross-spectra), and noise (half-ring difference map auto-spectra) of the 70, 100, and 143 GHz channels. As stated earlier, the 70–100 GHz channel comparison quantifies the cross-instrument consistency of *Planck*.

This description of the statistics of noise contributions to the empirical cross-spectra derived from the *Planck* sky maps sets up the analysis of inter-frequency consistency of *Planck* data. The pure instrumental noise contribution to the empirical cross-spectra is very small over a large ℓ-range for the HFI channels, and at 70 GHz over the ℓ-range of the first peak in the spectrum, where we now focus our analysis. Cosmic variance is irrelevant for our discussion because we are assessing inter-frequency

data consistency, and the instruments observe the same CMB anisotropy. Any possible departures from complete consistency of the measurements must be accounted for by frequency-dependent foreground emission, accurate accounting of systematic effects, or (at a very low level) residual noise.

3.2. Spectral consistency

Figure 6 shows spectra of the 70, 100, and 143 GHz maps for the three sky masks, differences with respect to the *Planck* 2013 best-fit model, and ratios of different frequencies. In the ℓ-range of the first peak and below, the 143/100 ratio shows the effects of residual diffuse foreground emission outside the masks. The largest mask reduces the detected amplitude, but
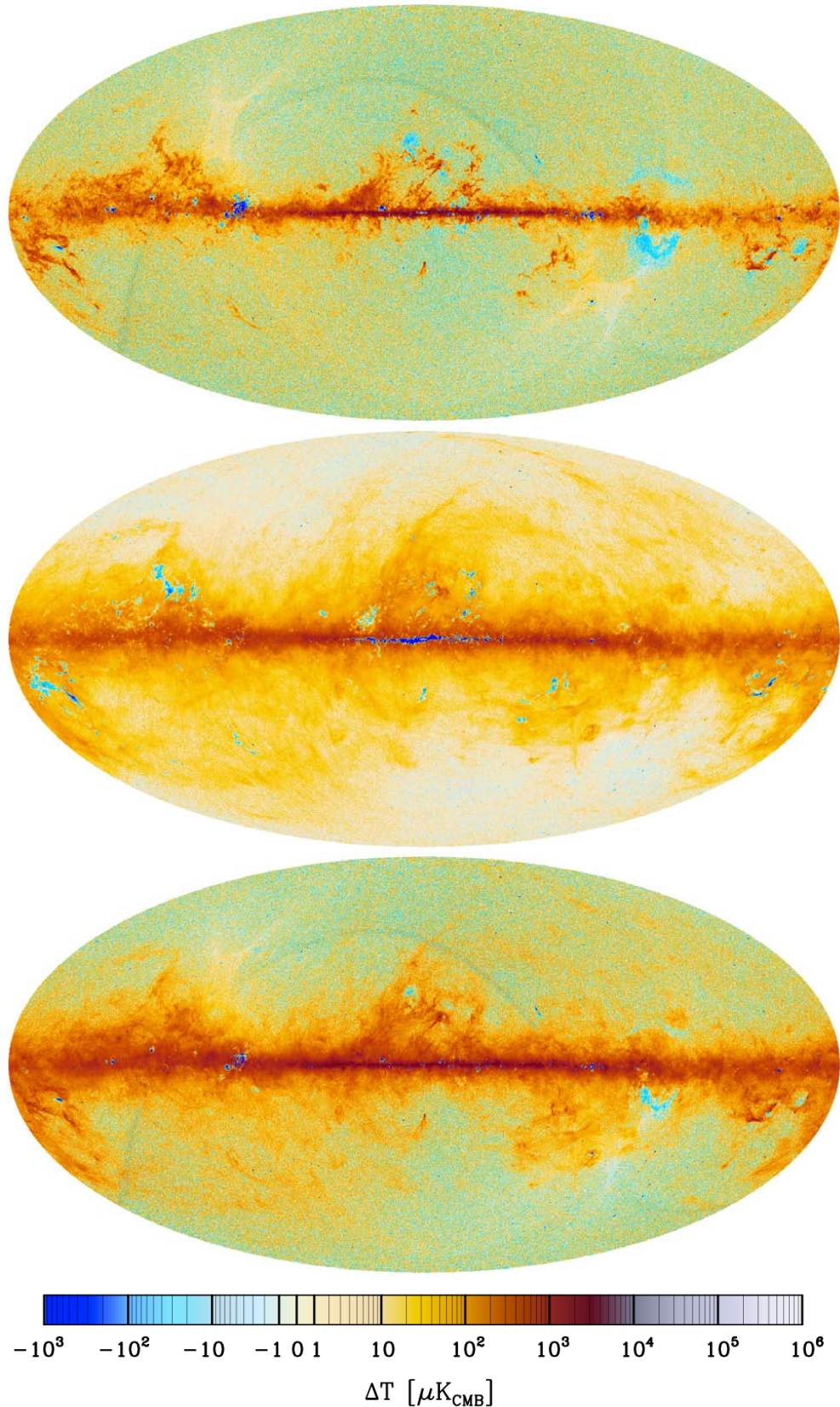
Fig. 3. Difference maps. *Top*: 100 GHz minus 70 GHz. *Middle*: 143 GHz minus 100 GHz. *Bottom*: 143 GHz minus 70 GHz. All sky maps are smoothed to angular resolution FWHM = 15′ by a filter that accounts for the difference between the effective beam response at each frequency and a Gaussian of FWHM 15′. These maps illustrate clearly the difference in the noise level of the individual maps, excellent overall nulling of the CMB anisotropy signal, and frequency-dependent foregrounds. The 100–70 difference shows predominantly CO ($J = 0 \rightarrow 1$) emission (positive) and free-free emission (negative). The 143–100 difference shows dust emission (positive) and CO emission (negative). The 143–70 difference shows dust emission (positive) and free-free emission (negative). The darker stripe in the top and bottom maps is due to reduced integration time in the 70 GHz channel in the first days of observation (see Planck Collaboration II 2014, Sect. 9.5).

Table 1. Rms values of the unmasked regions of the frequency and difference maps shown in Fig. A.1, and for the $f_{sky} = 69.4\%$, 59.6%, and 39.7% masks shown in Fig. 1.

|		rms [μK]					
		70 GHz		100 GHz		143 GHz	
ν	f_{sky}	Freq.	Diff.	Freq.	Diff.	Freq.	Diff.
	39.7%	90.44	28.62	29.01	28.93	29.00	28.69
70 GHz	59.6%	90.09	29.48	29.66	29.47	29.77	29.22
	69.4%	90.12	29.46	29.79	29.36	30.03	29.12
	39.7%	. . .	. . .	85.63	4.27	5.49	4.76
100 GHz	59.6%	. . .	. . .	85.05	4.38	6.09	4.83
	69.4%	. . .	. . .	85.16	4.39	6.76	4.81
	39.7%	. . .	. . .	. . .	. . .	85.70	2.11
143 GHz	59.6%	. . .	. . .	. . .	. . .	85.23	2.17
	69.4%	. . .	. . .	. . .	. . .	85.45	2.18

Notes. Diagonal blocks give the rms values for half-ring sums ("Freq.") and differences ("Diff.") of single-frequency maps. Off-diagonal blocks give the same quantities for frequency-*difference* maps (70 GHz−100 GHz, 70 GHz−143 GHz, and 100 GHz−143 GHz). As described in the text, the maps are smoothed to a common resolution of 15′, somewhat lower than the resolution of the 70 GHz maps. In addition, structure on scales larger than 8° is determined and removed from all maps to avoid introducing biases from residual monopoles and dipoles, so that only structure from 15′ to 8° in angular scale is included in these calculations.
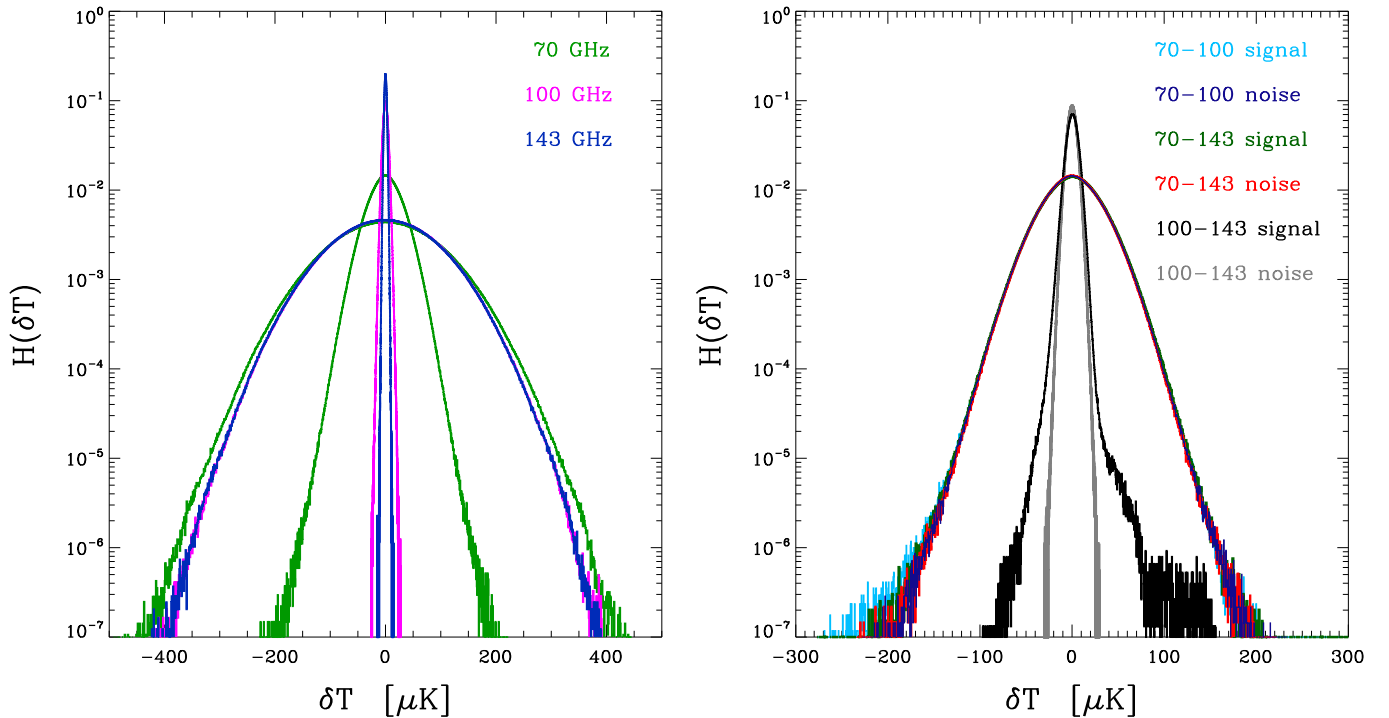
Fig. 4. Signal and noise for the frequency maps of Fig. 2 (*left panel*) and the difference maps of Fig. 3 (*right panel*), with the 59.6% mask in all cases. The broader, signal+noise curves are nearly Gaussian due to the dominant CMB anisotropies. The 70 GHz curve is broader than the 100 and 143 GHz curves because of the higher noise level, but is still signal-dominated for $|dT/T| \gtrsim 50 \mu$K. The narrower noise curves, derived from the half-ring difference maps, are not Gaussian because of the scanning-induced spatial dependence of pixel noise in *Planck* maps. The considerably higher noise level of the 70 GHz map is again apparent. The histograms of the difference maps show noise domination near the peak of each pair of curves (the signal+noise and noise curves overlap). The pairs involving 70 GHz are wider and dominated by the 70 GHz noise, but the wings at low pixel counts show the signature of foregrounds that exceed the noise levels, primarily dust and CO emission in the negative wing, and free-free and synchrotron emission in the positive wing. In the low-noise 100 minus 143 GHz pairs, the signal, due mostly to dust emission in the negative wing and to free-free and CO residuals in the positive wing, stands out clearly from the noise.

does not remove it completely. The frequency dependence of the ratios conforms to what is well known, namely, that diffuse foreground emission is at a minimum between 70 and 100 GHz. The 143/100 pair is more affected by diffuse foregrounds than the 70/100 pair, as the dust emission gets brighter at 143 GHz. The effects of residual unresolved foregrounds in Fig. 6 are discussed in the next section.

Near the first acoustic peak, measurements in the three *Planck* channels agree to better than one percent of the CMB signal, and to much better than their uncertainties, which are dominated by the effects of cosmic/sample variance (see Fig. 6). Inclusion of cosmic/sample variance is essential for making inferences about the underlying statistical processes of the Universe; however, since the receivers at all frequencies are
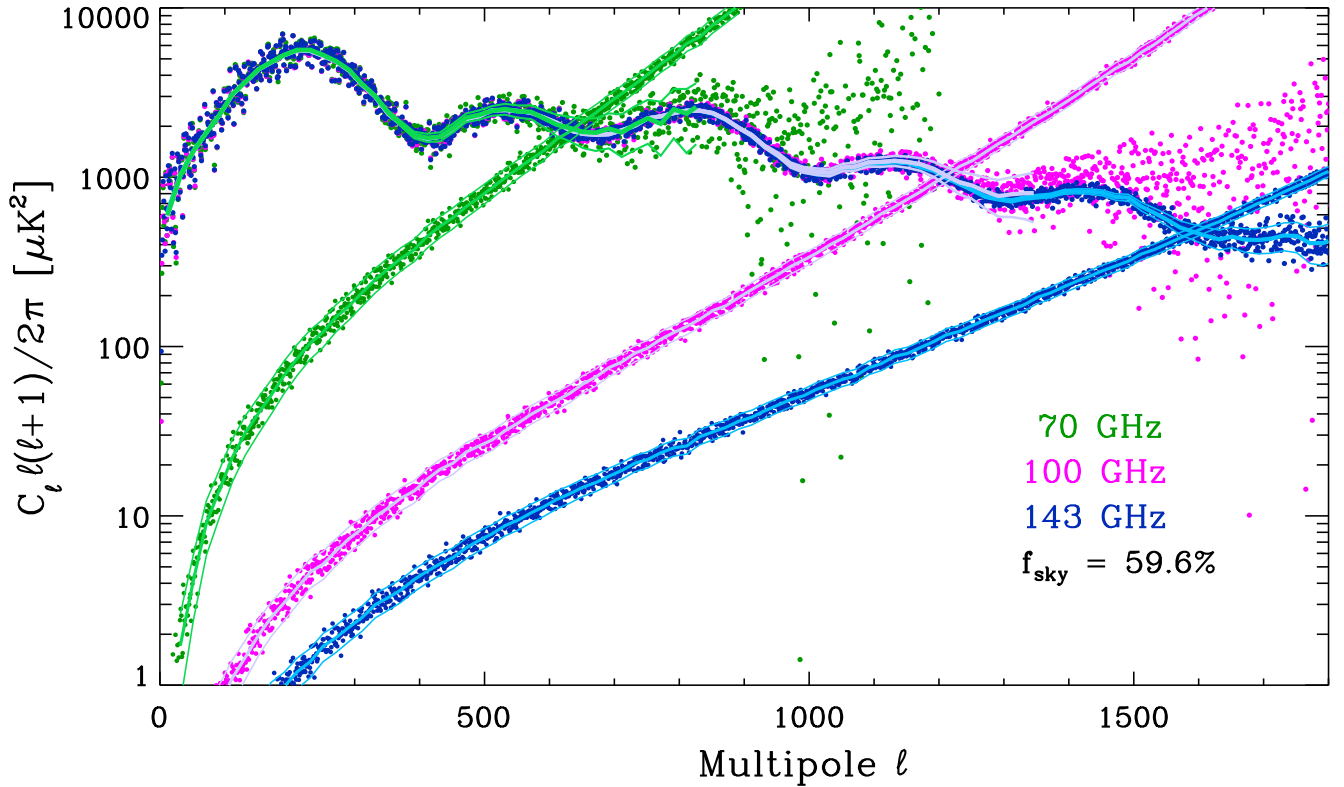
Fig. 5. *Planck* 70, 100, and 143 GHz CMB anisotropy power spectra computed for the GAL060 mask. Mask- and beam-deconvolved cross-spectra of the half-ring maps show the signal; auto-correlation spectra of the half-ring difference maps show the noise. Points show single multipoles up to $\ell = 1200$ for 70 GHz and $\ell = 1700$ for 100 and 143 GHz. Heavy solid lines show $\Delta \ell = 20$ boxcar averages. The S/N near the first peak ($\ell = 220$) is approximately 80, 1900, and 6000 for 70, 100, and 143 GHz, respectively. Noise power is calculated according to the large-ℓ approximation, i.e., as a $\chi^2_{2\ell+1}$ distribution with mean C_ℓ and rms $C_\ell[f_{\text{sky}}(2\ell + 1)/2]^{-1/2}$. Pairs of thin lines mark $\pm 3\sigma$ bands of noise power around the noise spectra. We translate this statistical spread of noise power C_ℓs into the signal spectra estimated via half-ring map cross-spectra. Under the simplifying assumption that each C_ℓ of the noise in the cross-spectrum at high-ℓ is distributed as a sum of $(2\ell + 1)$ products of independent Gaussian deviates, each with variance $2C_\ell^{\text{noise}}$ derived from the half-ring difference maps, the Gaussianized high-ℓ noise in the cross-spectra has zero mean and rms of $2C_\ell^{\text{noise}}[f_{\text{sky}}(2\ell + 1)]^{-1/2}$. Pairs of thin lines mark $\pm 1\sigma$ bands of noise around the boxcar-averaged cross-spectra.

observing a single realization of the CMB, cosmic variance is irrelevant in the comparison of the measurements themselves. Figure 7 is the same as the top two middle panels of Fig. 6 (i.e., over 60% of the sky), but *without* inclusion of cosmic/sample variance in the uncertainties. As can be seen, cosmic/sample variance completely dominates the measurement uncertainties up to multipoles of 400, after which noise dominates.

### 3.3. Residual unresolved sources

Figure 6 shows that while diffuse foregrounds are significant for low multipoles, they are much less important on smaller angular scales. To see clearly the intrinsic consistency between frequencies, however, we must remove the effects of unresolved sources.

Discrete extragalactic foregrounds comprise synchrotron radio sources, Sunyaev-Zeldovich (SZ) emission in clusters, and dust emission in galaxies. These have complicated behaviour in ℓ and ν. All have a Poisson part, but the SZ and cosmic infrared background sources also have a correlated part. These are the dominant foregrounds (for a 39.7% Galactic mask) for $\ell \gtrsim 200$. For frequencies in the range 70–143 GHz and multipoles in the range 50–200, they stay below 0.2%. The minimum in unresolved foregrounds remains at 143 GHz, with less than 2% contamination up to $\ell = 1000$.

Discrete sources detected above 5σ in the PCCS (Planck Collaboration XXVIII 2014) are individually masked, as described in Sect. 2. Corrections for residual unresolved radio sources are determined by fitting the differential Euclidean-normalized number counts $S^{5/2}dN/dS$ in Jy$^{1.5}$ sr^{-1} at each frequency with a double power law plus Euclidean term:

$$S^{5/2}\,\mathrm{d}N/\mathrm{d}S = \frac{A_{\text{f}}S^{5/2}}{[(S/S_1)^{b_{\text{f1}}} + (S/S_2)^{b_{\text{f2}}}] + A_{\text{E}}(1 - \mathrm{e}^{-S/S_{\text{E}}})}, \quad (1)$$

where A_{f} is the amplitude at faint flux density levels, S_1 is the first faint flux density level, b_{f1} is the exponent of the first power law at faint flux densities, S_2 is the second faint flux density level, b_{f2} is the exponent of the second power law at faint flux densities, A_{E} is the amplitude of the Euclidean part, i.e., at large flux density, and S_{E} is the flux density level for the Euclidean part ($\gtrsim 1$ Jy). These are then integrated from a cutoff flux density corresponding to the 5σ selection limit in the PCCS at 143 GHz, and the equivalent levels for a radio source with $S \propto \nu^{-0.7}$ at 100 and 70 GHz. Thermal SZ and CIB fluctuations are fitted as part of likelihood function determination described in Planck Collaboration XV (2014); the values found there are used here. Figure 8 shows the level of these corrections, while Fig. 9 shows the ratios of power spectra after the corrections are made.
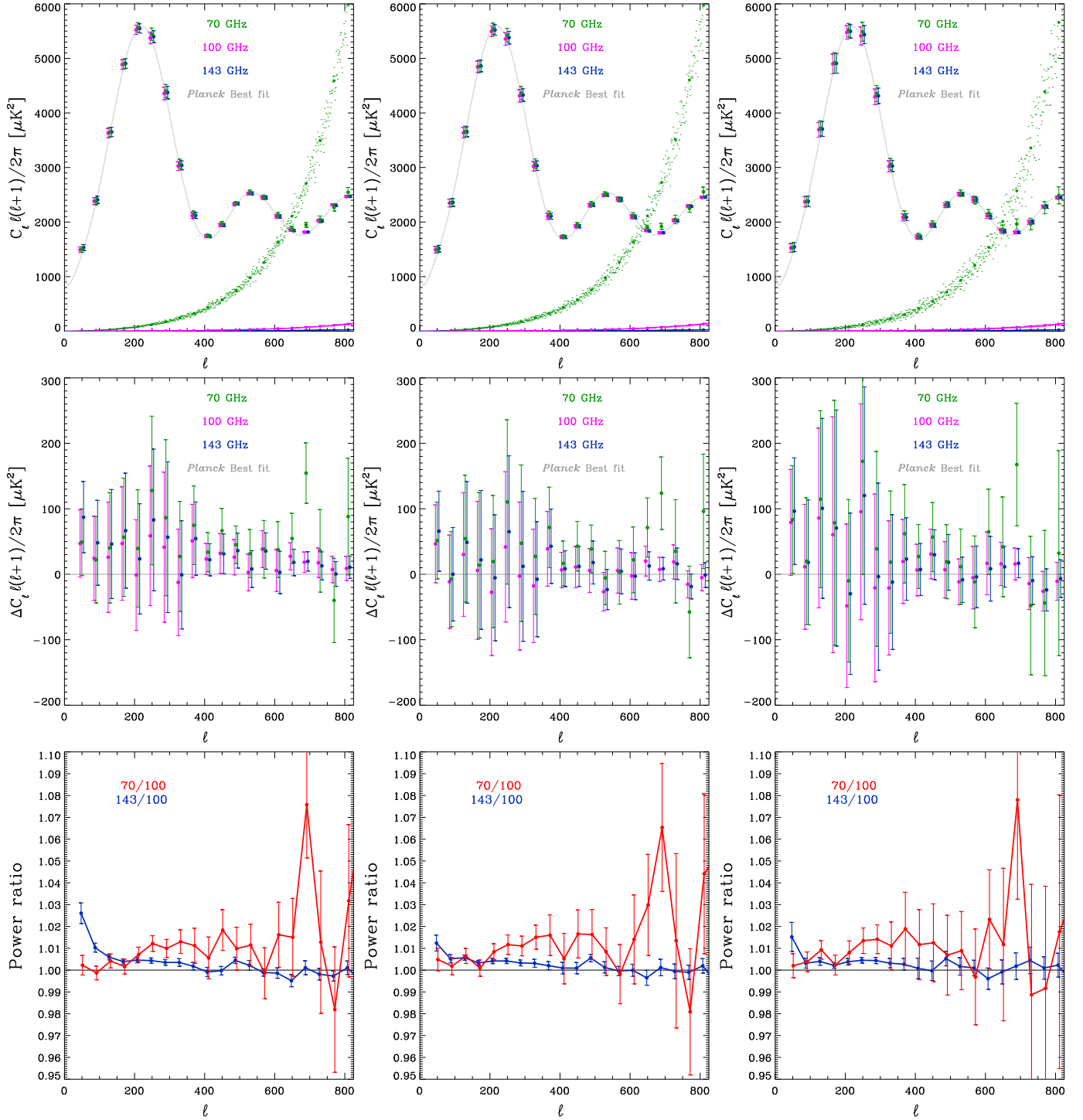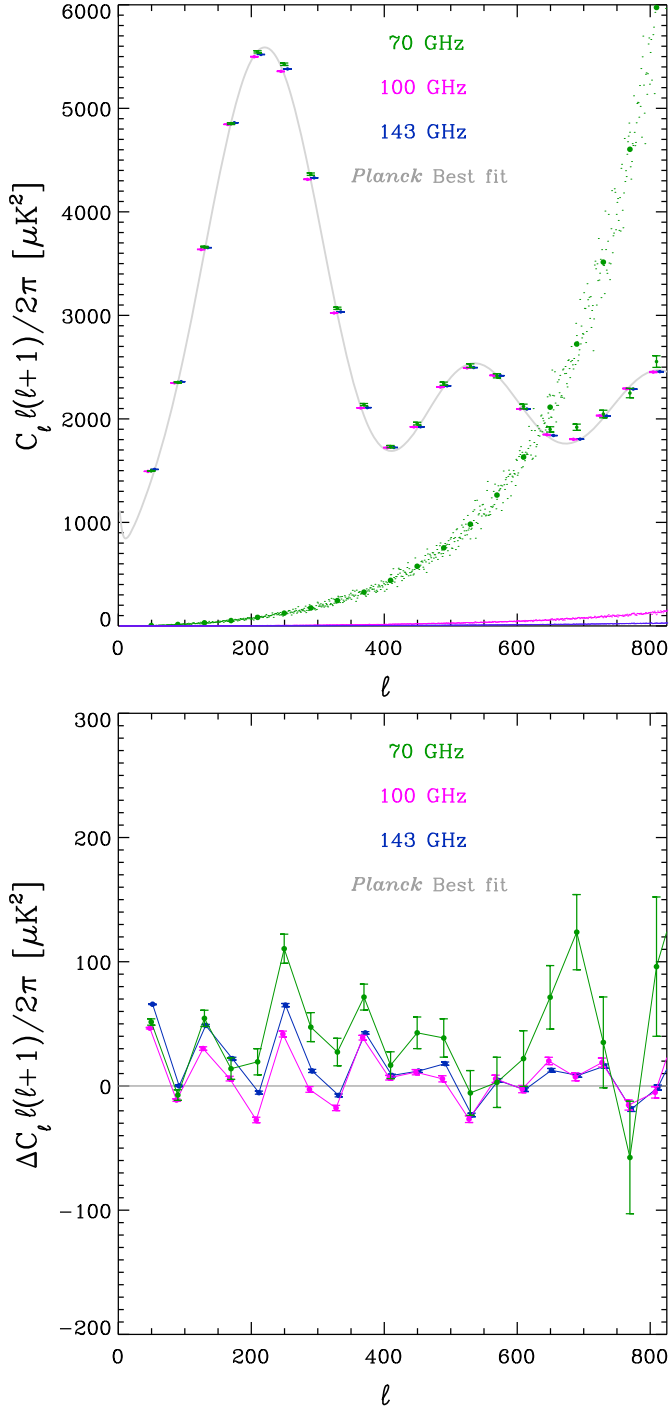
Fig. 6. Spectral analysis of the *Planck* 70, 100, and 143 GHz maps. Columns show results computed using the three sky masks in Fig. 1, with, from left to right, f_{sky} = 69.4%, 59.6%, and 39.7%. *Top row*: CMB anisotropy spectra binned over a range of multipoles $\Delta\ell = 40$, for $\ell \geq 30$, with $(2\ell + 1)$-weighting applied within the bin. Error bars are computed as a measure of the rms-power within each bin, and hence comprise both the measurement inaccuracy and cosmic variance. The grey curve is the best-fit *Planck* 6-parameter ΛCDM model from Planck Collaboration XVI (2014). Noise spectra computed from the half-ring-difference maps are shown: for the 70 GHz channel, the $S/N \approx 1$ at $\ell \approx 650$. *Middle row*: residuals of the same power spectra with respect to the *Planck* best-fit model. *Bottom row*: power ratios for the 70 vs. 100 GHz and 143 vs. 100 GHz channels of *Planck*. The ratios are calculated ℓ by ℓ, then binned. The error bars show the standard error of the mean for the bin. The effect of diffuse foregrounds is clearly seen in the changes in the 143/100 ratio with sky fraction at $\ell \approx 100$. Bin-to-bin variations in the exact values of the ratios with sky fraction emphasize the importance of making such comparisons precisely.

3.4. Assessment

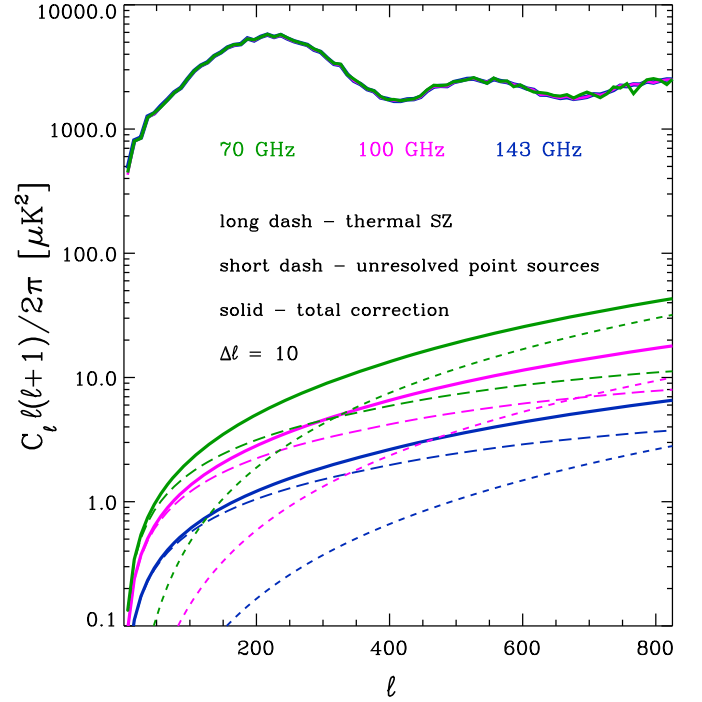The 70/100 and 143/100 ratios in Fig. 9, for 59.6% of the sky, averaged over the range $70 \leq \ell \leq 390$ where the 70 GHz signal-to-noise ratio (S/N) is high, are 1.0080 and 1.0045, respectively. Over the range $70 \leq \ell \leq 830$, the ratios are 1.0094 and 1.0043, respectively. Table 2 collects these ratios and following ones for easy comparison.

Fig. 8. Estimates of the residual thermal SZ and unresolved radio and infrared source residuals that must be removed.
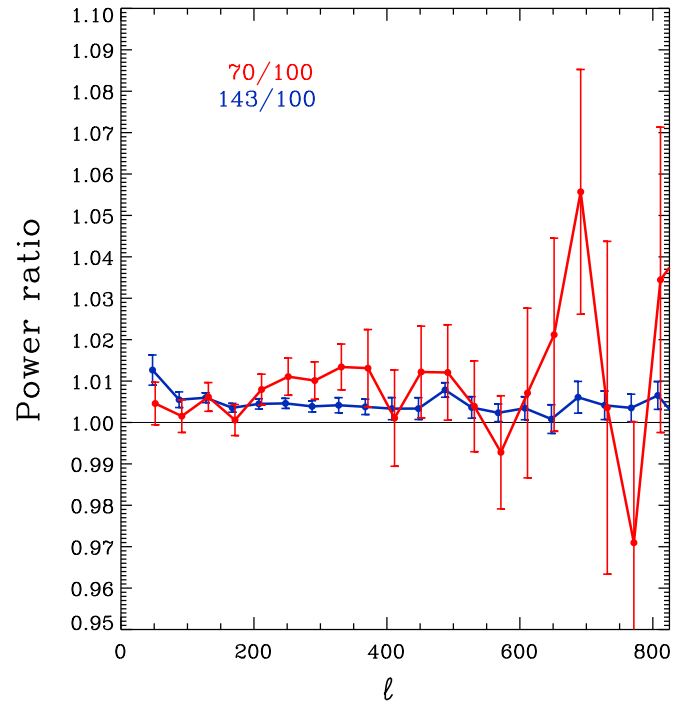

Fig. 7. Same as the top two panels of the middle column of Fig. 6, but *without* inclusion of signal cosmic variance in the uncertainties. Both signal × noise and noise × noise terms are included.

Fig. 9. Same as the bottom middle panel of Fig. 6, but corrected for differences in unresolved-source residuals (see text). We have not tried to account for uncertainties in the foreground correction itself; however, since the correction is small, the effect on the uncertainties would be small.

Section 7.4 of Planck Collaboration VI (2014) uses the SMICA code to intercalibrate on the common CMB anisotropies themselves, with results given in Fig. 35 of that paper. For 40% of the sky, the 70/100 and 143/100 power ratios are 1.006 and 1.002 over the range $50 \leq \ell \leq 300$, and 1.0075 and 1.002 over the range $300 \leq \ell \leq 700$. (These *gain* ratios from Fig. 35 of Planck Collaboration VI 2014 must be squared for comparison with the *power* ratios discussed in this section and given in Table 2.) The SMICA equivalent power ratios are systematically about 0.2% closer to unity than those calculated in this section;

however, in broad terms the two methods give remarkably similar results. Moreover, the absolute *gain* calibration uncertainties given in Planck Collaboration V (2014, Table 8) and Planck Collaboration VIII (2014) are 0.62% for 70 GHz and 0.54% for 100 GHz and 143 GHz. The agreement at the power spectrum

level between 70, 100, and 143 GHz is quite reasonable in terms of these overall uncertainties. We will return to comparisons of spectra in Sects. 4 and 5.

We are working continuously to refine our understanding of the instrument characteristics, implement more accurate calibration procedures, and understand and control systematic effects better. All of these will lead to reduced errors and uncertainties in 2014. In the next section we describe an analysis of beams and calibration procedures that has already been beneficial.

4. Beams, beam transfer functions, and calibration

The residual differences that we see in Sect. 3 are small but not negligible. We now address the question of whether they may be due to beam or calibration errors. Detailed descriptions and analyses of the LFI and HFI beams and calibration are contained in Planck Collaboration IV (2014), Planck Collaboration V (2014), Planck Collaboration VII (2014), and Planck Collaboration VIII (2014). In this section we summarize our present understanding of calibration and beam effects for the two instruments, explain the reasons for the approximations that have been made in data processing, provide estimates for the impact of these approximations on the resulting maps and power spectra, and outline plans for changes to be implemented in the 2014 data release. We will show that the small differences between LFI and HFI at intermediate ℓ seen in Fig. 9 are significantly reduced by improvements in our understanding of the near sidelobes in HFI, which affect the window functions in this ℓ range.

4.1. Beam definitions

Calibration of the CMB channels (30 to 353 GHz) is based on the dipole anisotropies produced by the motion of the Sun relative to the CMB and of the modulation of this dipole by the motion of the spacecraft relative to the Sun (which we refer to as the solar and orbital dipoles, respectively). For the 2013 data release and all LFI and HFI frequency channels considered in this paper, the time-ordered data have been fit to the solar dipole as measured by WMAP (Hinshaw et al. 2009). The present analysis aims to show that the LFI-HFI differences at intermediate ℓ seen in Fig. 9 are understood within the present uncertainties due to beams, calibration, and detector noise. Planck Collaboration IV (2014) and Planck Collaboration VII (2014) define three regions of the beam response (see Fig. 10, Fig. 1 of Planck Collaboration IV 2014, and Fig. 5 of Tauber et al. 2010), as follows.

The nominal beam or main beam is that portion used to create the beam window functions for the 2013 data release. The nominal beam carries most of the beam shape information and more than 99% of the total solid angle, and therefore has most of the information needed for the 2013 cosmological analysis. The angle from the beam centre to the boundary of the nominal beam varies with frequency and instrument, and is 1°9, 1°3, and 0°9 for 30, 44, and 70 GHz, respectively, and 0°5 for 100 GHz and above.

The near sidelobes comprise any effective solid angle within 5° of the centre of the beam that is *not* included in the nominal beam. The response to the dipole from this region of the beam is very similar to that from the nominal beam, and unaccounted-for near sidelobe response leads to errors in the window function.

The far sidelobes comprise the beam response more than 5° from the centre. Because of the geometry of the telescope and baffles, the bulk of this solid angle is at large angles from the line of sight, not far from the spin axis, and not in phase with
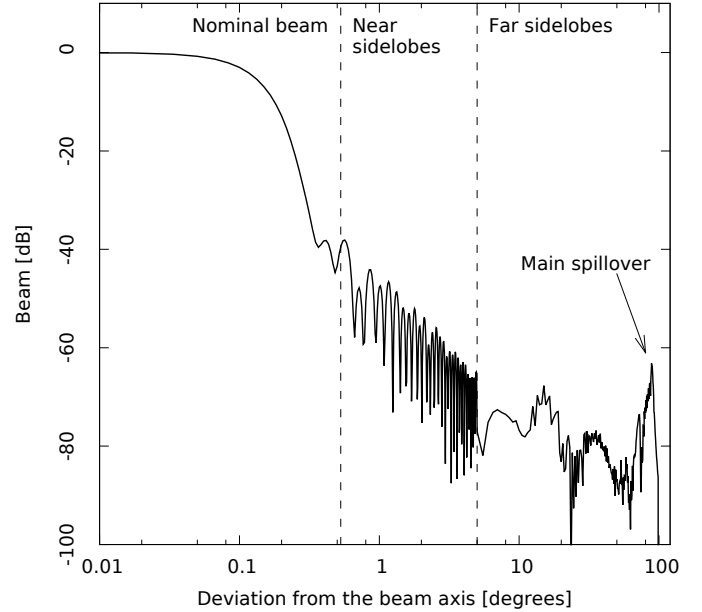
Fig. 10. Radial slice through a 70 GHz beam from the GRASP model, illustrating the nominal beam, near sidelobe, and far sidelobe regions. The exact choice of angular cutoff for the nominal beam is different for different frequencies.

the dipole seen in the nominal beam, and therefore has little effect on the dipole calibration. However, the secondary mirror spillover, containing typically 1/3 of the total power in the far sidelobes, is in phase with the dipole, and affects the calibration signal. The inaccuracy introduced by approximating the optical response with the nominal beam normalized to unity is corrected to first order by our use of a pencil (δ-function) beam to estimate the calibration.

For reference, for the 2013 release we estimated a contribution to the solid angle from near sidelobes of 0.08%, 0.2%, and 0.2%, and from far sidelobes of 0.62%, 0.33%, and 0.31%, for 70, 100, and 143 GHz, respectively, of which 0.12%, 0.075%, and 0.055% is from the secondary spillover referred to above. Recent analysis, detailed in Appendix C, has resulted in a new estimate for the near sidelobe contribution for 100 and 143 GHz of $0.30 \pm 0.2\%$ and $0.35 \pm 0.1\%$, respectively[7]. The impact of this is described below.

4.2. Nominal beam approximation

In the 2013 analysis, both LFI and HFI performed a "nominal beam" calibration, i.e., we assumed that the detector response to the dipole can be approximated by the response of the nominal beam alone, which in turn is modelled as a pencil beam (for details see Appendix B). Clearly, if 100% of the power were contained in the nominal beam, the window function would fully account for beam effects in the reconstructed map and power spectrum. In reality, however, a fraction of the beam power is missing from the nominal beam and appears in the near and far sidelobes, affecting the map and power spectrum reconstruction in ways that depend on the level of coupling of the sidelobes with the dipole. Accordingly, a correction factor is applied that has the form (see Eq. (B.12))

$$T_{\text{sky}} \approx \widetilde{T}_{\text{sky}} \left(1 - \phi_{\text{sky}} + \phi_D \right), \tag{2}$$

---

[7] The nominal beam solid angle statistical errors are 0.53% and 0.14% at 100 and 143 GHz, respectively.

Table 2. Summary of ratios of *Planck* 70, 100, and 143 GHz power spectra appearing in this paper.

Location	Features	f_{sky}	ℓ Range	Spectrum Ratios 70/100	143/100
Sect. 3.4, Fig. 6, bottom centre . . .	No corrections	59.6%	$70 \le \ell \le 390$	1.0089	1.0039
			$70 \le \ell \le 830$	1.0140	1.0020
Sect. 3.4, Fig. 9	DSR^a correction	59.6%	$70 \le \ell \le 390$	1.0080	1.0045
			$70 \le \ell \le 830$	1.0094	1.0043
Sect. 3.4, SMICA	Paper VI, Fig. 35	40%^{d}	$50 \le \ell \le 300$	1.0060	1.0020
			$300 \le \ell \le 700$	1.0075	1.0020
Sect. 4.3, Fig. 12	NS^c correction	59.6%	$70 \le \ell \le 390$	1.0052	1.0040
			$70 \le \ell \le 830$	1.0077	1.0020
Sect. 4.3, Fig. 13	DSR^a +NS^c corrections	59.6%	$70 \le \ell \le 390$	1.0043	1.0046
			$70 \le \ell \le 830$	1.0032	1.0043
Sect. 5, Fig. 14	CamSpecLikelihood^d	. . .	. . .	. . .	1.00058

Notes. $^{(a)}$ Discrete-source residual correction. $^{(b)}$ The mask used in Paper VI, Fig. 35 was similar but not identical to the 39.7% mask of Fig. 1. The differences do not affect the comparison. $^{(c)}$ Near sidelobe correction, 100 and 143 GHz. $^{(d)}$ Planck Collaboration XVI (2014).
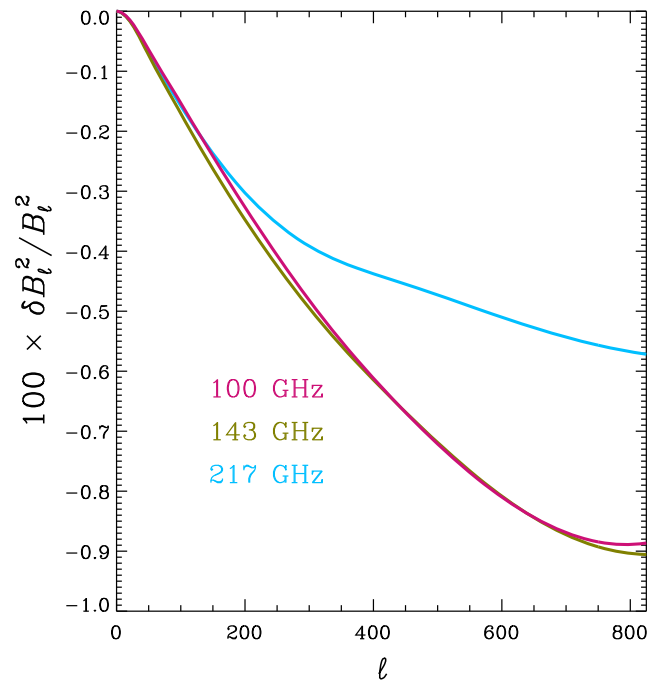
where T_{sky} is the true sky temperature, $\widetilde{T}_{sky}$ is the sky temperature estimated by the "nominal beam" calibration, $\phi_D \equiv (P_{side} * D)/(P_{nominal} * D)$ is the coupling of the (near and far) sidelobes with the dipole, and $\phi_{sky} \equiv (P_{side} * T_{sky})/\widetilde{T}_{sky}$ is a small term (of order 0.05%, see Appendix C) representing the sidelobe coupling with all-sky sources other than the dipole (mainly CMB anisotropies and Galactic emission). The term ϕ_D is potentially important, since dipole signals contributing to the near sidelobes may bias the dipole calibration. Our current understanding of the value and uncertainty of the scale factors $\eta = \left(1 - \phi_{sky} + \phi_D\right)$ for LFI and HFI is discussed in detail in Appendix C.

4.3. Key findings

There are two key findings or conclusions from the analyses in Appendices B and C.

– For LFI, a complete accounting of the corrections using the *current* full 4π beam model would lead to an adjustment of about 0.1% in the amplitude of the released maps (i.e., 0.2% of the power spectra). At present this is an estimate, and rather than adjusting the maps we include this in our uncertainty.
– For HFI, recent work on a *hybrid beam profile*, including data from planet measurements and GRASP[8] modelling, has led to improvements in the beam window function correction rising from 0 to 0.8, 0.8, 0.5, and 1.2% over the range $\ell = 1$ to $\ell = 600$, at 100, 143, 217, and 353 GHz, respectively. Uncertainties in these corrections have not been fully characterized, but are dominated by the intercalibration of Mars and Jupiter data and are comparable to the corrections themselves (see Fig. C.3).

Figure 11 shows the corrections to the beam window functions at 100, 143, and 217 GHz. Figure 12 shows the effect of those corrections on the 70/100 and 143/100 power spectrum ratios, uncorrected for unresolved source residuals. There is almost no effect on the 100/143 GHz ratio, as the *differential* beam window function correction between these two frequencies is small. The 70/100 ratio, however, is significantly closer to unity. In

---
[8]   Developed by TICRA (Copenhagen, DK) for analysing general reflector antennas (http://www.ticra.it).

Fig. 11. Effective beam window function corrections from Fig. C.3, which correct for the effect of near-sidelobe power missing in the HFI beams used in the 2013 results (Sect. C.2.1). Uncertainties are not shown here for clarity, but are shown in Fig. C.3, and would be large on the scale of this plot. The 217 GHz correction is shown for illustration only.
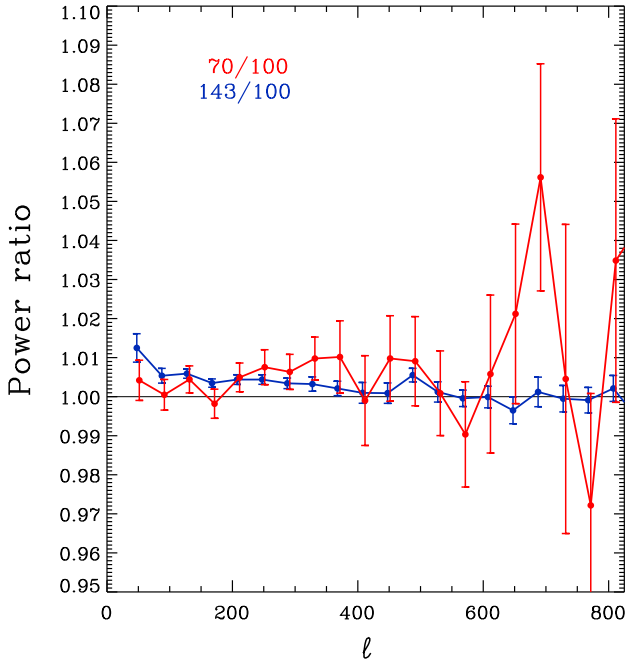
Sect. 5, we show that such a correction does not materially affect the 2013 cosmology results.

Figure 13 shows the power spectrum ratios corrected for both the beam window functions and unresolved source residuals (Sect. 3.3). The average ratios over the range $70 \le \ell \le 390$ are 1.0043 and 1.0046 for 70/100 and 143/100, respectively. For the range $70 \le \ell \le 830$, they are 1.0032 and 1.0043.

For the 2014 release, we expect internal consistency and uncertainties to further improve as more detailed models of the beam and correction factors are included in the analysis.

We have concentrated in this section on beam effects; however, the transfer function depends also on the residuals of the time transfer function, measured on planets and glitches, and

Fig. 12. Same as the bottom middle panel of Fig. 6, but corrected for the near-sidelobe power at 100 and 143 GHz that was not included in the 2013 results. Since the beam corrections for 100 and 143 GHz are nearly identical, the ratio 143/100 hardly changes. The ratio 70/100, however, changes significantly, moving towards unity. Uncertainties in the beam window function corrections are not included.
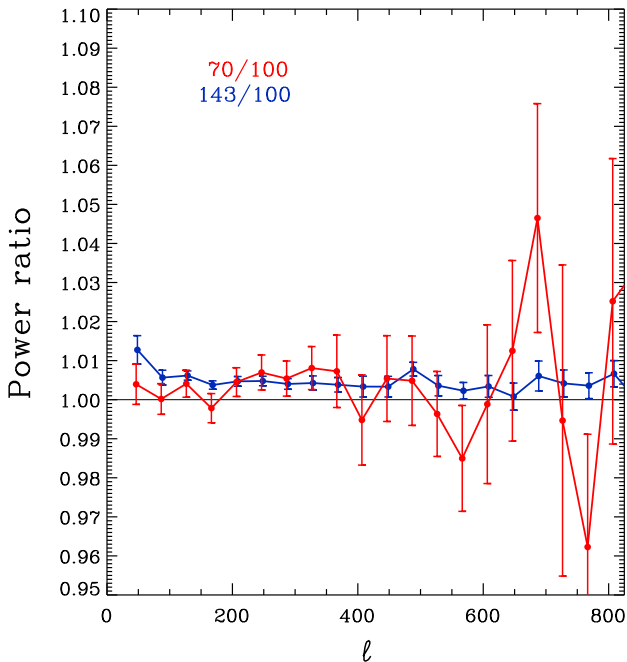
Fig. 13. Same as the bottom middle panel of Fig. 6, but corrected for both the near-sidelobe power at 100 and 143 GHz that was not included in the 2013 results and for unresolved source residuals (Sect. 3.3). Uncertainties in the beam window function corrections are not included.

deconvolved in the time-ordered data prior to mapmaking and calibration. For the HFI channels, the transfer function used for the 2013 cosmological analysis assumes that all remaining effects are contained within a $40' \times 40'$ map of a compact scanning beam and corresponding effective beam. Any residuals from uncorrected time constants longer than 1 s are left in the maps, and

will affect the dipoles and thus the absolute calibration. This has been investigated since the 2013 data release; time constants in the 1–3 s range have been identified and shown to be the origin of difficulties encountered with calibration based on the orbital dipole. The 2014 data release will include a correction of these effects, and the absolute calibration will be carried out on the orbital dipole. A reduction in calibration uncertainties by a factor of a few can be anticipated.

5. Likelihood analysis

In the previous section we showed how work since release of the 2013 *Planck* results has led to an improved understanding of the beams and a small (and well within the stated uncertainties) revision to the near-sidelobe power in the HFI beams, which brings HFI and LFI into even closer agreement. In this section, we show that the revision in the HFI beams has little effect on cosmological parameters. To do this, we make use of the likelihood and parameter estimation machinery described in Planck Collaboration XV (2014) and Planck Collaboration XVI (2014). For both analytical and historical reasons there are differences (e.g., masks, frequencies, multipole ranges) in the analyses in this section and in previous sections; however, as will be seen, the effects of the differences are accounted for straightforwardly, and do not affect the conclusions about parameters.

The *Planck* 2013 cosmological parameter results given in Planck Collaboration XVI (2014) are determined for $\ell \geq 50$ from 100, 143, and 217 GHz "detector set" data described in Planck Collaboration XV (2014, Table 1), by means of the `CamSpec` likelihood analysis described in the same paper that solves simultaneously for calibration, foreground, and beam parameters. This approach allows power spectrum comparisons to sub-percent level precision, using only cross-spectra (as in Sect. 3) to avoid the need for accurate subtraction of noise in auto-spectra.

In this section, we determine the ratios of the 100, 143, and 217 GHz spectra using this approach, and compare the 143/100 results to those found in Sect. 3. We show that the apparent difference in the results from the two different approaches is easily accounted for by differences in the sky used, the difference between the detector set data and full frequency channel data, and the use of individual detector recalibration factors in the detector set/likelihood approach. Having established essentially exact correspondence between the methods, we use the likelihood machinery to estimate the effect on cosmological parameters of the revision in the near-sidelobe power in the HFI beams.

In Planck Collaboration XVI (2014), we used mask G45 ($f_{sky} = 0.45$) for 100×100 GHz, and mask G35 ($f_{sky} = 0.37$) for 143×143 GHz and 217×217 GHz to control diffuse foregrounds. However, here we are interested in precise tests of inter-frequency power spectrum consistency, so (as before) we need to compute spectra using exactly the same masks to cancel the effects of cosmic variance from the primordial CMB. We have therefore recomputed all of the spectra using mask G22 ($f_{sky} = 0.22$) and mask G35, restricting the sky area to reduce the effects of Galactic dust emission at 143 and 217 GHz. The spectra are computed from means of detector set cross-spectra Planck Collaboration XV (2014). For each spectrum, we subtract the best-fitting foreground model from the Planck+WP+high-ℓ solution for the base six-parameter ΛCDM model with parameters as tabulated in Planck Collaboration XVI (2014), and correct for the best-fit relative calibration factors of this solution. The convention adopted in the `CamSpec` likelihood fixes
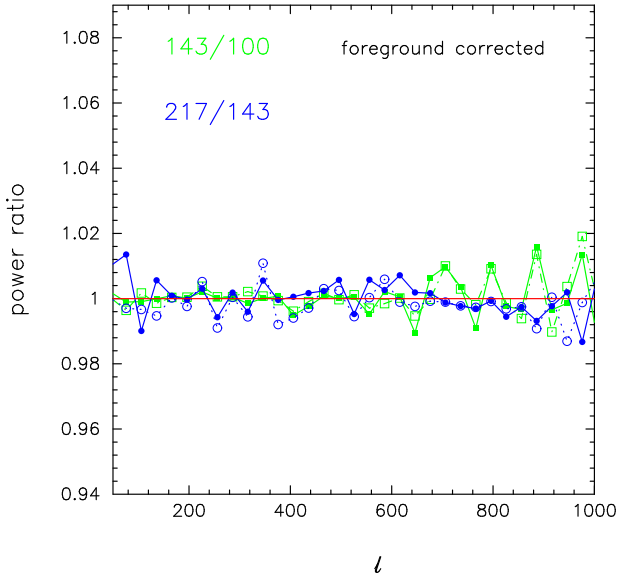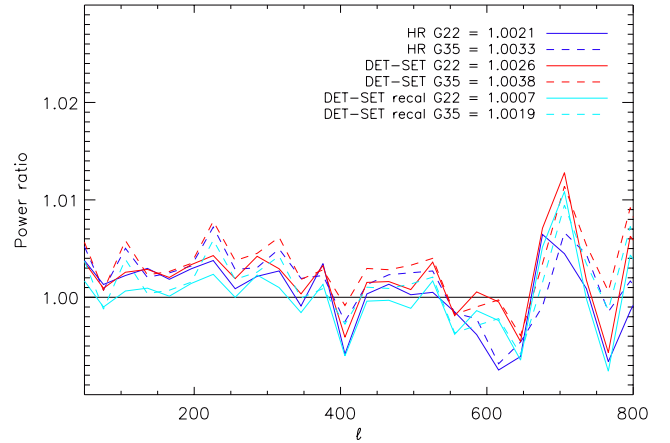
Fig. 14. Ratios of 100, 143, and 217 GHz power spectra calculated from detector sets with the likelihood method, including subtraction of the best-fitting foreground model (see text) and correction for the best-fit relative calibration factors for individual detectors. Solid symbols and lines show ratios for mask G22; open symbols and dotted or dashed lines show ratios for mask G35. The greater scatter in 217/143 for mask G35 is caused by CMB-foreground cross-correlations.


Fig. 15. Effects on the 143/100 ratio of changes in the mask, choice of detectors, and detector recalibration. Solid lines indicate ratios calculated with mask G22; dashed lines indicate mask G35. Use of detector sets gives the cyan curves with recalibration turned on and the red curves with recalibration turned off. Use of full-frequency half-ring cross spectra, as in Sect. 3, gives the blue curves. The cyan curves are comparable to the green curves in Fig. 14, which also have intra-frequency calibration and foreground corrections applied. The blue-dashed curve agrees extremely well with the blue curve in the bottom right panel of Fig. 6, as it should (see text).

the calibration of 143×143 to unity, hence calibration factors multiply the 100×100 and 217×217 power spectra to match the 143×143 spectrum. The best fit values of these coefficients are $c_{100} = 1.00058$ and $c_{217} = 0.9974$ for mask G22, both very close to unity and consistent with the calibration differences between individual detectors at the same frequency (see Table 3 of Planck Collaboration XV 2014). The results are shown in Fig. 14.

The 143/100 ratio given by the dashed green line can be compared with the bottom right panel of Fig. 6, which is based on 40% of the sky, nearly the same as mask G35. As expected, they are not identical; Fig. 15 explains the differences. In Fig. 15, pairs of curves in the same colour show the difference between mask G22 and mask G35, as labelled. The cyan curves can be compared to the green curves in Fig. 14, which also have inter-frequency calibration and foreground corrections applied. The red curves show the effect of turning off detector-by-detector intercalibration. The blue curves show the effect of switching from detector sets to full-frequency half-ring cross spectra (as in Sect. 3). The progression from solid cyan to dashed blue in Fig. 15 shows the relationship between the PLA map-based results and the detector-set/likelihood results. As used in the likelihood analysis (Planck Collaboration XV 2014), the 143/100 ratio is 1.00058 over the full ℓ range used in the likelihood analysis, compared to the ratios between 1.0039 and 1.0046 seen in Table 2 over $70 \le \ell \le 390$ for Figs. 6, 9, 12, or 13. However, using mask G35 ($f_{sky} = 0.37$), using half-ring cross-spectra of full-frequency detector sets, and turning off unresolved-source residual and detector-by-detector intercalibration factors, changes the ratio over $60 < \ell < 390$ to 1.0033, in good agreement with the 1.0039 calculated for the 143/100 comparison in the bottom right panel of Fig. 6.

This agreement extends to the detailed shapes of the two curves (blue in the bottom right panel of Fig. 6 and blue-dashed in Fig. 15) as well. This is necessarily the case, since they are both cross-spectra of half-ring frequency maps, without corrections for unresolved-source residuals, and using the "2013"

beams. The only difference in the data comes from the masks used, which are the GAL040 mask ($f_{sky} = 39.7\%$) and mask G35 ($f_{sky} = 37\%$), respectively. This agreement is nevertheless reassuring in showing that the differences in spectral ratios between the PLA map-based approach and the detector set likelihood approach are well-understood, and disappear for common data and masks.

We can now turn to the question of whether the small revision to the HFI beams affects cosmological parameters. A full revised beam analysis at the detector level that includes the 0.1% power in near sidelobes not taken into account directly in the 100 and 143 GHz beams in 2013 (Sect. 4) has not yet been completed; however, for an indicative test, we rescaled the averaged cross-spectra appearing in the likelihood by functions corresponding to the new beam shapes for the ℓ-ranges for which they have been calculated (presently up to $\ell = 2000$). Where necessary the shapes were extrapolated as being flat up to higher ℓ. The 143×217 spectrum was rescaled by the geometric mean of the 143 and 217 rescalings. Then we performed a Monte Carlo Markov Chain (MCMC) analysis for the base ΛCDM model for the modified "high-ℓ" likelihood with an unmodified low-ℓ Planck likelihood and WMAP low-ℓ polarized likelihood ("WP"). To see any change in the beam error behaviour, we choose to sample explicitly over all twenty of the eigenmode amplitudes, rather than sampling over one and marginalizing over the other nineteen, as we did in the parameters paper (Planck Collaboration XVI 2014).

The results are indicated in Figs. 16 and 17, showing a selection of cosmological parameters and the beam eigenmode amplitudes, respectively. As expected, we see a boost in the power spectrum amplitude, resulting in a change to the cosmological amplitude at about the 1σ level. However, the largest shift in any other cosmological parameter is 0.3σ. The uncertainty in the beam window function is described by a small number of eigenmodes in multipole space and their covariance matrix (Planck Collaboration VII 2014). The posteriors for the first beam eigenmodes for the 100, 143, and 217 effective spectra shift noticeably; others are practically unchanged. The beams
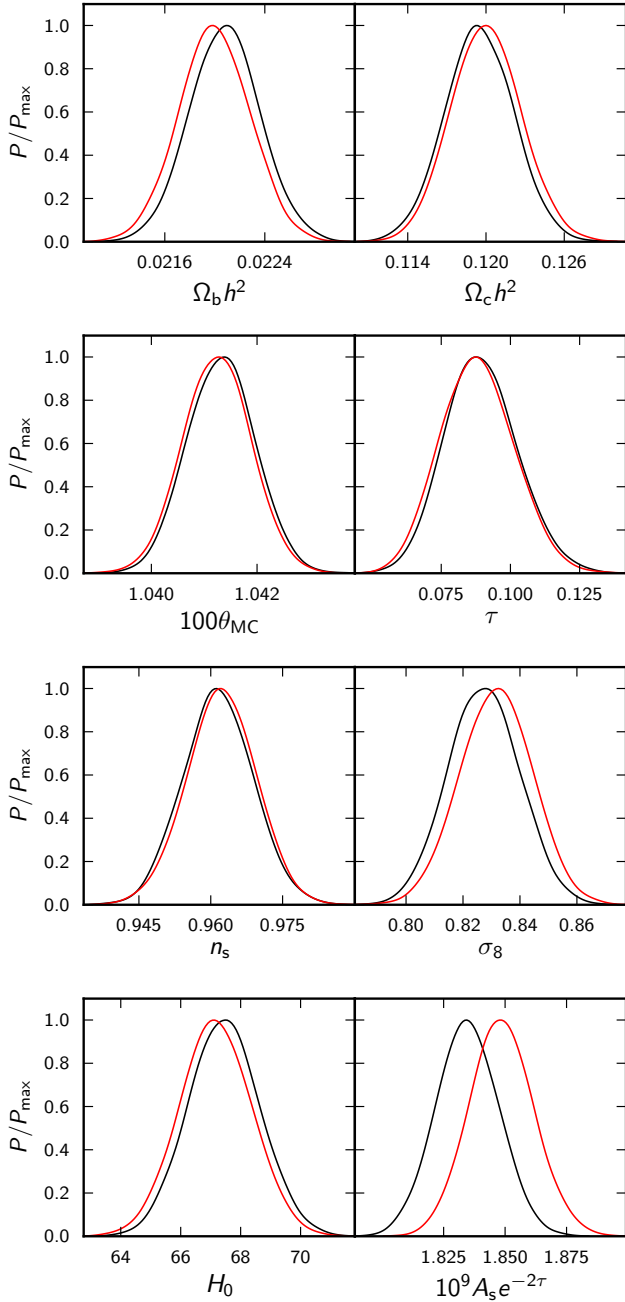
Fig. 16. Changes in cosmological parameters from the inclusion of the near sidelobe power discussed in the text. The black curves are the 2013 results for *Planck* plus the low-ℓ WMAP polarization (WP). The red curves are for *Planck*+WP using the revised HFI beams. The shifts in the posteriors are all less than 0.3σ except for the cosmological amplitude A_s and parameters related to it, as expected.

used here are preliminary and the beam eigenmodes have not been generated self-consistently to match the beam calibration pipeline. No adjustment was made in the calibration of the low-ℓ likelihood. Nevertheless, from the results presented here, we can anticipate that the 2014 revisions to the beams will affect the overall calibration of the spectra, but will have little other impact on cosmology.

6. Comparison of *Planck* and WMAP

Planck and WMAP have both produced sky maps with excellent large-scale stability, as demonstrated by many null tests both internal to the data and external. In this section, we compare

Planck and WMAP measurements in several different ways. In Sect. 6.1, we compare power spectra calculated from 70 and 100 GHz *Planck* maps available in the PLA, and from *V*- and *W*-band yearly maps in the WMAP9 data release. In Sect. 6.2, we perform a likelihood analysis similar to that in Sect. 5 and in Planck Collaboration XVI (2014), and show that the differences between the map-based and likelihood analyses are well-understood. In Sect. 6.3 we assess the results in the context of the uncertainties for the two experiments.

6.1. Map and power spectrum analysis

The WMAP9 data release includes $N_{\rm side} = 1024$ yearly sky maps from individual differential assemblies (DAs), both corrected for foregrounds and uncorrected, as well as $N_{\rm side} = 512$ frequency maps. WMAP uses somewhat different sky masks than *Planck*. In Sect. 3 we emphasized the importance of using exactly the same masks in comparing results. Accordingly, for *Planck*/WMAP comparisons we construct a joint mask, taking the union of the *Planck* GAL060 mask used in Sects. 3 and 4, the WMAP KQ85 mask, which imposes larger cuts for radio sources and some galaxy clusters, as required by the poorer angular resolution of WMAP, and the *Planck* joint 143, 100, 70 GHz point source mask. Fig. 18 shows the mask, which leaves $f_{\rm sky} = 56.7\%$ of the sky available for spectral analysis.

We use the same spectrum estimation procedure as in Sect. 3, evaluating the relevant cross-spectra, correcting for the mask with the appropriate kernel, and dividing out the relevant beam response and pixel smoothing functions. As the mask is different from the one used for *Planck*-only comparisons, so is the mask-correction kernel. All maps are analysed using the same mask.

For WMAP, there are nine yearly sky maps for each differential assembly V1, V2, W1, W2, W3, and W4, at $N_{\rm side} = 1024$. Because the WMAP *V* band and the *Planck* 70 GHz band are so close in frequency, as are *W* band and 100 GHz, we use maps not corrected for foregrounds for the comparison. All possible cross spectra from the yearly maps and differential assemblies are computed (630 at *W* band, 153 at *V*), and corrected for the mask, beam (using WMAP beam response functions, different for each differential assembly), and pixel-smoothing. The corrected spectra are averaged, and the error on the mean is computed for each C_ℓ. These average differential-assembly spectra are then co-added with inverse noise weighting to form one *V* band and one *W* band spectrum. These are binned ($\ell_{\rm min} = 30$, $\Delta\ell = 40$), and rms errors in the bin values are computed. The resulting spectra are shown in Fig. 19.

The 70, 100, and 143 GHz *Planck* spectra and spectral ratios in Figs. 19–21 are determined as before, but using the new mask, starting from the 70 GHz $N_{\rm side} = 1024$ half-ring PLA maps and the 100 and 143 GHz $N_{\rm side} = 2048$ maps degraded to $N_{\rm side} = 1024$. Thus all spectra are evaluated with the identical mask, at the same resolution. Spectral binning and the estimation of rms bin errors proceed in exactly the same way as for the WMAP spectra and for previous *Planck*-only comparisons.

Figure 19 compares the *Planck* 70 GHz power spectrum with the WMAP *V*-band spectrum, and the *Planck* 100 GHz power spectrum with the WMAP W-band spectrum. The *Planck* 2013 best-fit model is shown for comparison. The *Planck* and WMAP9 spectra disagree noticeably in the ℓ-range of the first two peaks. Ratios of spectra in Fig. 20 show this disagreement directly. In Figs. 20–22 the 70/100 and 143/100 ratios are the same as in Sects. 3 and 4, except for the small change in the mask.
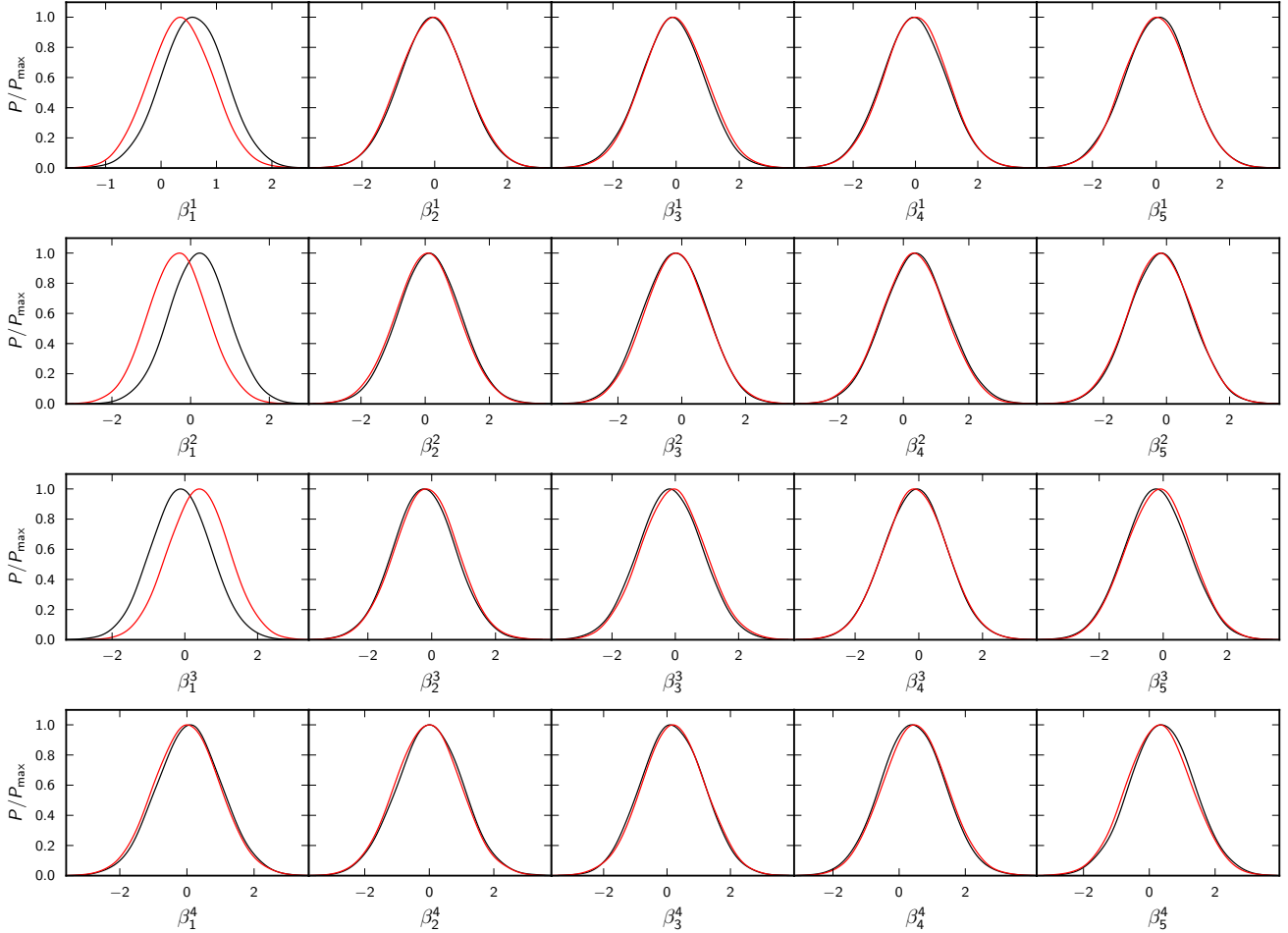
Fig. 17. Changes in the beam eigenmode coefficients from the inclusion of the near-sidelobe power now established but not included in the processing for the 2013 results. Black curves are for *Planck*+WP; red curves are for *Planck*+WP with the revised beams. The superscript indicates the effective spectrum (one to four for 100, 143, 217, and 143 × 217 respectively) while the subscript indicates eigenmode number.
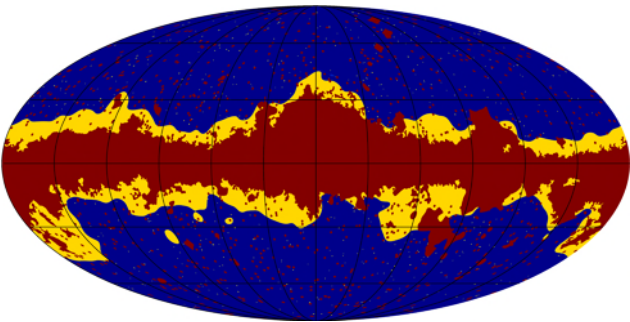
Fig. 18. *Planck* $f_{sky} \approx 60\%$ Galactic mask in yellow and WMAP KQ75 at $N_{side} = 1024$ in red. The mask used for comparative spectral analysis of the *Planck* 70, 100, and 143 GHz, and WMAP nine-year *V*- and *W*-band sky maps is the union of the two. The joint *Planck* 70, 100, and 143 GHz point source mask is also used, exactly as before. The final sky fraction is $f_{sky} = 56.7\%$. The *Planck* mask is degraded to the pixel resolution $N_{side} = 1024$, at which the yearly WMAP individual differential assembly maps are available.

Figure 21 is the same as Fig. 20, but with the *Planck* 70/100 and 143/100 ratios corrected for the missing near sidelobe power in the 100 and 143 GHz channels, discussed in Sect. 4.

Figure 22 is the same as Fig. 21, but with all spectra additionally corrected for residual unresolved sources, as described in Sect. 3.3. Mean values of the ratios over specified multipole ranges are given in Table 3.

6.2. Likelihood analysis

The likelihood analysis here is slightly different from the analysis presented in Sect. 5. First, we created a point source mask by concatenating the WMAP/70/100/143/217 point source catalogues. We present here only the results comparing WMAP, LFI 70 GHz, and HFI 100 GHz. Restricting the frequencies to a range close to the diffuse foreground minimum has the advantage that we can increase the sky area used. We therefore present results for mask G56 (unapodized), which leaves 56% of the sky. This mask, combined with the point source mask, is degraded in resolution from $N_{side} = 2048$ to the natural N_{side} for WMAP (512) and LFI (1024).

Beam-corrected spectra for the WMAP *V*, *W*, and *V* + *W* bands, and for the LFI 70 GHz bands were computed. Errors on these spectra were estimated from numerical simulations. At 70 GHz we have three maps of independent subsets of detectors, therefore we can estimate three pseudo-spectra by cross-correlating them by pairs. Pseudo-spectra are then mask- and beam-deconvolved. The final 70 GHz spectrum is obtained as a noise-weighted average of the cross-spectra. Noise variances are estimated from anisotropic, coloured noise MC maps for each set of detectors. We use the FEBeCoP effective beam window functions for each subset of detectors (the three pairs 18–23, 19–22, and 20–21 as defined in Planck Collaboration II 2014). In the present plots we do not show beam uncertainties, which are bounded to be $\Delta B_\ell / B_\ell \lesssim 0.2\%$
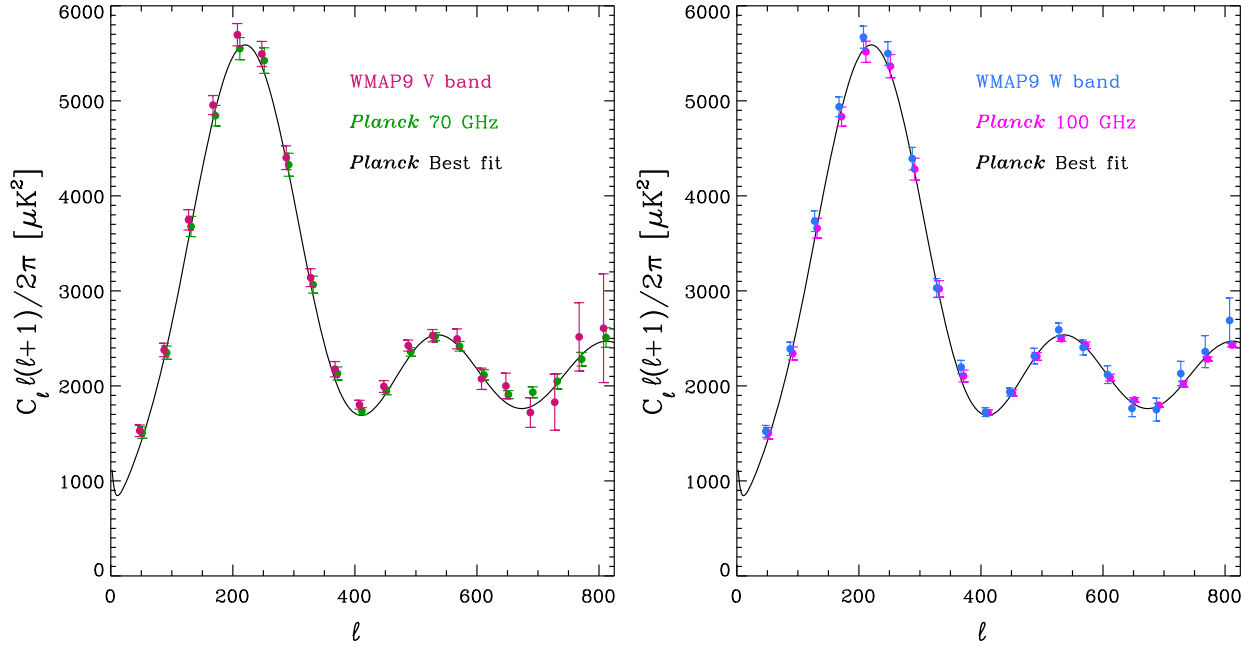
Fig. 19. *Left*: WMAP *V* band compared to *Planck* 70 GHz and best-fit model. *Right*: WMAP *W* band compared to *Planck* 100 GHz and best-fit model. The joint *Planck*/KQ75 sky mask + *Planck* point source mask ($f_{sky} = 56.7\%$; see Fig. 18) is used. Because the frequencies are so close, no corrections for foregrounds are made.
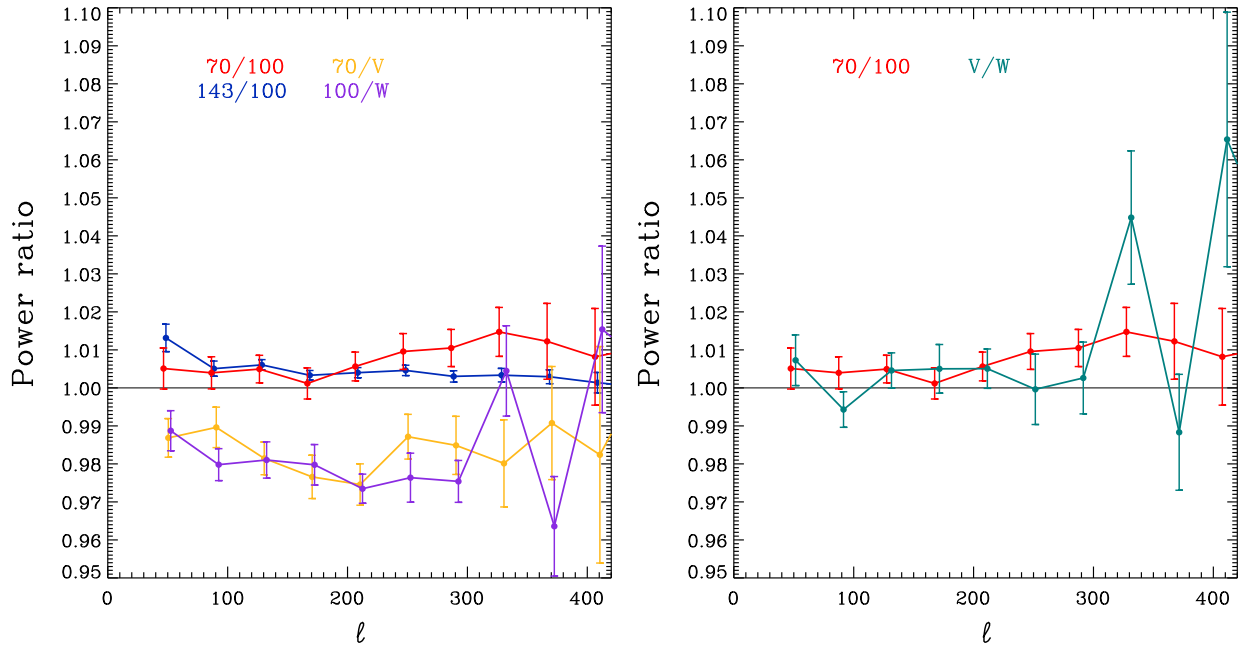
Fig. 20. Ratios of power spectra for *Planck* and WMAP over the joint *Planck*/KQ75+*Planck* point source mask with $f_{sky} = 56.7\%$. The *Planck* 70/100 and 143/100 ratios can be compared to the bottom middle panel in Fig. 6 for $f_{sky} = 59.6\%$. Here we limit the horizontal scale because the WMAP noise beyond $\ell = 400$ makes the ratios uninformative. The general shape of the *Planck* ratios is the same; however, it is clear (as it was in Fig. 6) that changes in the sky fraction change the ratios significantly within the uncertainties. This underscores the importance of strict equality of all factors in such comparisons.

in the multipole range considered here (Planck Collaboration VI 2014).

We also derive power spectra for the WMAP *V* and *W* bands, using coadded nine year maps per DA, for which no foreground cleaning has been attempted. There are two DA maps for *V*-band and four for *W*-band. The *V*-band spectrum is obtained by cross-correlating the two available maps, whereas the *W* spectrum is the noise-weighted average of the six spectra derived by correlating pairs of the four DA maps. We have produced Monte Carlo simulations of noise in order to assess the error bars of the WMAP spectra. We generate noise maps according to the pixel noise values provided by the WMAP team rescaled by the number of observations per pixel. Beam transfer functions per DA are those provided by the WMAP team. In the present error budget we did not include beam uncertainties, which would be $\Delta B_\ell / B_\ell \approx 0.4\%$ for *V* and 0.5% for *W*, over $\ell < 400$.

For LFI and WMAP, we subtract an unresolved thermal SZ template with the amplitude derived from the CamSpec
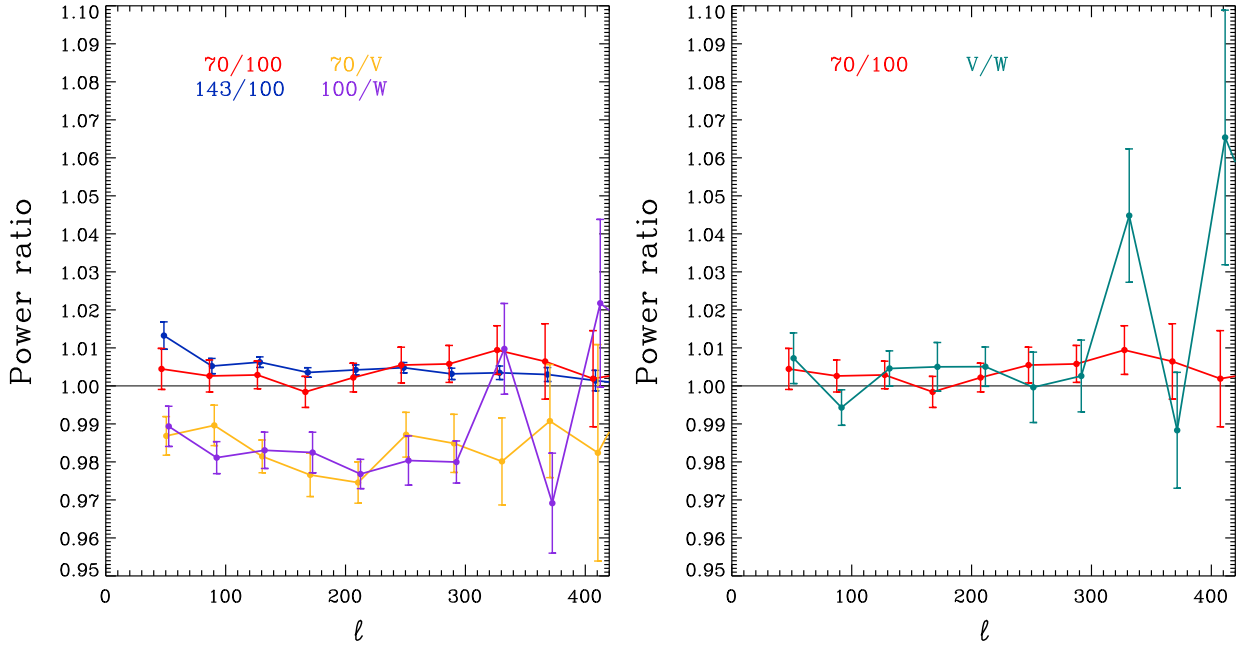
Fig. 21. Same as Fig. 20, but the *Planck* 70/100 and 143/100 ratios are corrected for beam power at 100 and 143 GHz that was not included in the effective beam window function used in the 2013 results.
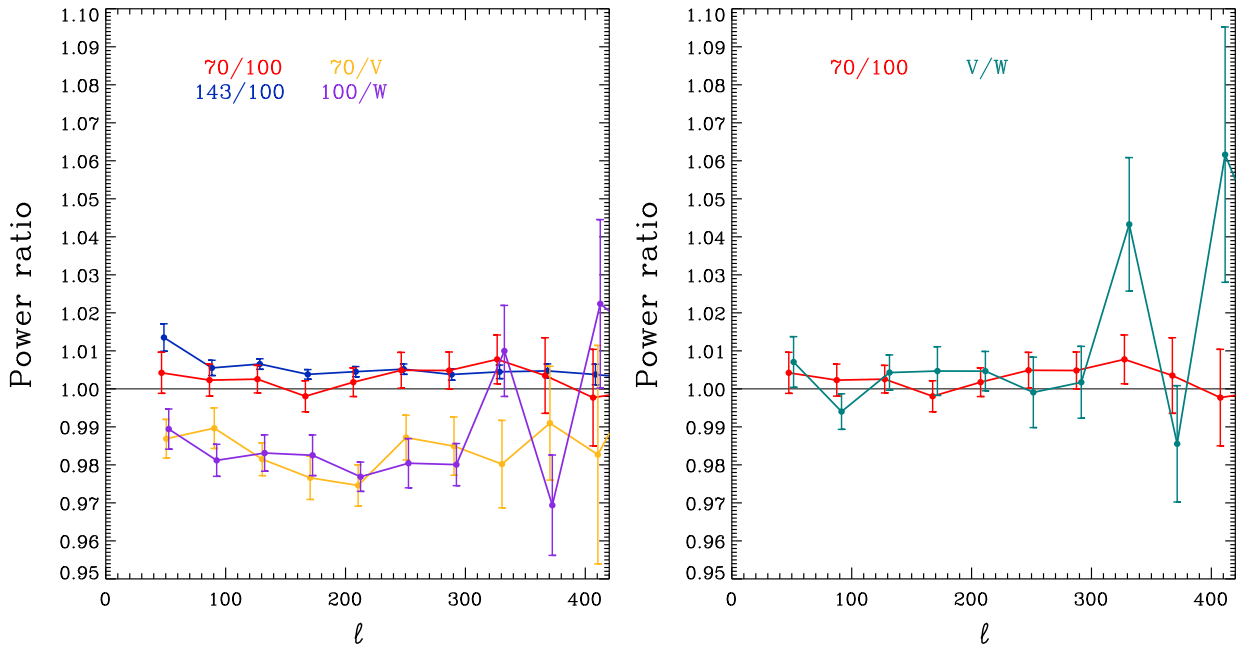
Fig. 22. Same as Fig. 20, but including corrections for both *Planck* beams and for *Planck* and WMAP unresolved-source residuals.

likelihood analysis, which we extrapolate to the central LFI and WMAP frequencies. We also subtract a Poisson point source term with an amplitude chosen to minimize the variance between the measured spectra and the best-fit theoretical model at high multipoles. We then determine calibration factors c_X for the WMAP and 70 GHz LFI spectrum relative to the 100 GHz HFI spectrum by minimizing

$$\chi^2 = \sum_b \frac{(\mathcal{D}_b^{100} - c_X \mathcal{D}_b^X)^2}{(\sigma_{Xb}^2 + \sigma_I^2)}, \tag{3}$$

until convergence, at each iteration determining σ_I, an "excess scatter" term, by requiring that the reduced χ^2 be unity. (The excess scatter comes primarily from foreground-CMB correlations, as discussed in Planck Collaboration XV 2014.) The sum

extends over bins with central multipole in the range $50 \leq \ell \leq 400$. The index X denotes the spectrum (70, V, W, or $V + W$), and σ_{Xb} is the noise contribution to the error in band b. The spectra $\mathcal{D}$ in Eq. (3) are foreground-corrected. Calibration factors c_X and resulting spectra for 70 GHz, V, W, and $V + W$-band relative to 100 GHz are given in Fig. 23 and Table 3. The value of $c_{70} = 0.994$ seen in Fig. 23 is entirely consistent with the 70/100 ratios given in Sect. 5, taking into account mask and dataset variations as discussed in Sect. 5. A calibration factor for V relative to 70 GHz calculated the same way ($\mathcal{D}_b^{100}$ is replaced by $\mathcal{D}_b^{70}$ in Eq. (3)) is also included in Table 3.

To compare the likelihood results with the map-based ones, we need to identify the closest cases for which results are given. No correction for near sidelobes at 100 GHz (Sect. 4.3) was

Table 3. Summary of ratios of *Planck* 70 and 100 GHz and WMAP *V*- and *W*-band power spectra appearing in this paper.

Location	Features	f_{sky}	ℓ Range	Spectrum ratios		
				70/V	100/W	100/(V + W)
Sect. 6.1, Fig. 20	No corrections	56.7%	$70 \leq \ell \leq 390$	0.983	0.979	. . .
			$110 \leq \ell \leq 310$	0.981	0.977	. . .
Sect. 6.1, Fig. 21	Near-sidelobe (NS) correction, 100 GHz	56.7%	$70 \leq \ell \leq 390$	0.983	0.983	. . .
			$110 \leq \ell \leq 310$	0.981	0.981	. . .
Sect. 6.1, Fig. 22	Discrete-source residual+NS corrections	56.7%	$70 \leq \ell \leq 390$	0.983	0.983	. . .
			$110 \leq \ell \leq 310$	0.981	0.981	. . .
Sect. 6.2	Likelihood "calibration factor"; WMAP full-mission maps at N_{side} = 512 rather than yearly maps at N_{side} = 1024; *Planck* detector sets (see Sect. 5) rather than full-frequency half-ring data.	56.7%	$50 \leq \ell \leq 400$	0.978	0.976	0.974

included in the likelihood results, but corrections for residual unresolved sources were. On the other hand, from the results shown in Table 3, residual-source corrections make negligible difference. In the likelihood approach, ℓ values beyond about 300 will be significantly down-weighted due to increased variance. Thus the most reasonable comparison is between the ratios from the map-based approach in the ℓ range $110 \leq \ell \leq 310$ with no corrections, and the corresponding calibration factors from the likelihood approach. Values in Table 3 show good agreement between the two analyses. We have furthermore noticed that using the WMAP full-mission maps at resolution N_{side} = 512 rather than the yearly maps at N_{side} = 1024, and *Planck* detector sets rather than full-frequency half-ring maps, can lower the spectral ratio by 0.2% in the multipole range $110 \leq \ell \leq 310$.

6.3. Assessment

Both the direct comparison of power spectra from the 2013 results maps and the likelihood analysis show a discrepancy between *Planck* and WMAP across the region of the first peak, where the S/N for WMAP is good. This difference is about 2% in power, corresponding to 1% in the maps. These numbers quantify what can be seen by eye in Fig. 19. The result is roughly the same for comparisons of 70 GHz with *V*-band and 100 GHz with *W*-band, where the frequency differences are small enough to rule out foregrounds as the cause. There is some variation of the ratio with ℓ (perhaps seen more easily in Fig. 23), suggesting that the cause is not simply a result of calibration errors, but neither does the shape correspond obviously to what would be expected from missing power in beams.

The 70/V and 100/W ratios differ from unity by more than expected from the uncertainties in absolute calibration determined for *Planck* and WMAP. Calibration of WMAP9 is based on the orbital dipole (i.e., the modulation of the solar dipole due to the Earth's orbital motion around the Sun), with overall calibration uncertainty 0.2% (Bennett et al. 2013). The absolute calibration of the *Planck* 2013 results is based on the solar dipole (Sect. 1), assuming the WMAP5 value of $(369.0 \pm 0.9)\,\mathrm{km\,s^{-1}}$, where the 0.24% uncertainty includes the 0.2% absolute calibration uncertainty (Hinshaw et al. 2009). The overall calibration uncertainty is 0.62% in the 70 GHz maps and 0.54% in the 100 and 143 GHz maps (Planck Collaboration I 2014, Table 6). When comparing *Planck* and WMAP calibrated maps, one must remove from these uncertainties the 0.2% contribution of the WMAP absolute calibration uncertainty to the WMAP dipole, which thus affects both LFI and HFI equally. The remaining

0.14% uncertainty in the WMAP dipole (mostly due to foregrounds; Hinshaw et al. 2009) affects *Planck* but not WMAP, because its absolute calibration is from the orbital dipole. In the planned 2014 release, the *Planck* absolute calibration will be based on the orbital dipole, bypassing uncertainties in the solar dipole. At the power spectrum level for comparison with WMAP, then, the *Planck* uncertainty would be between $2 \times (0.54-0.2)\% = 0.68\%$ and $2 \times (0.62-0.2)\% = 0.84\%$, and the WMAP uncertainty 0.4%. The power spectrum ratios in Table 3 from Fig. 21 and Sect. 6.2 then represent a 1.5–2σ difference.

As the primary calibration reference used by *Planck* in the 2013 results is the WMAP solar dipole, the inconsistency between *Planck* and WMAP is unlikely to be the result of simple calibration factors. Reinforcing this conclusion is the fact that the intercalibration comparison given in Fig. 35 of Planck Collaboration VI (2014) for CMB anisotropies shows agreement between channels to better than 0.5% over the range 70–217 GHz, and 1% over all channels from 44 to 353 GHz, using 143 GHz as a reference. Problems with transfer functions are more likely to be the cause. The larger deviations at higher multipoles in the *Planck* intercalibration comparison just referred to also point towards transfer function problems.

Comparisons between WMAP- and LFI-derived brightness temperatures of Jupiter presented in Fig. 21 of Planck Collaboration V (2014) provide a potentially useful clue: the two instruments seem to agree (for a simple linear spectral model for Jupiter) within 1%, and much better than this at 70 GHz. The LFI points are derived from just two Jupiter transits. We now have eight transits in hand. If the full analysis of all the Jupiter crossings shows similar consistency with WMAP brightness temperatures, subtle effects from beam asymmetries and near sidelobes in the two instruments, rather than gross errors in main beam solid angles, may be the cause.

At present, we do not have an explanation for the $\approx$2% calibration difference between WMAP and *Planck*. The differences between WMAP and *Planck* are primarily multiplicative in the power spectra, and so have little impact on cosmological parameters other than on the amplitude of the primordial spectrum A_s. Figure 23 shows that after the spectra are rescaled by multiplicative factors, there is excellent *point-to-point* agreement between the LFI, HFI, and WMAP power spectra. Appendix A of Planck Collaboration XVI (2014) also shows explicitly that by restricting the Planck 2013 likelihood to ℓ_{max} = 1000, we recover almost identical cosmological parameters to those from WMAP apart from a small shift in A_s reflecting the calibration differences between the two experiments. Any shape differences
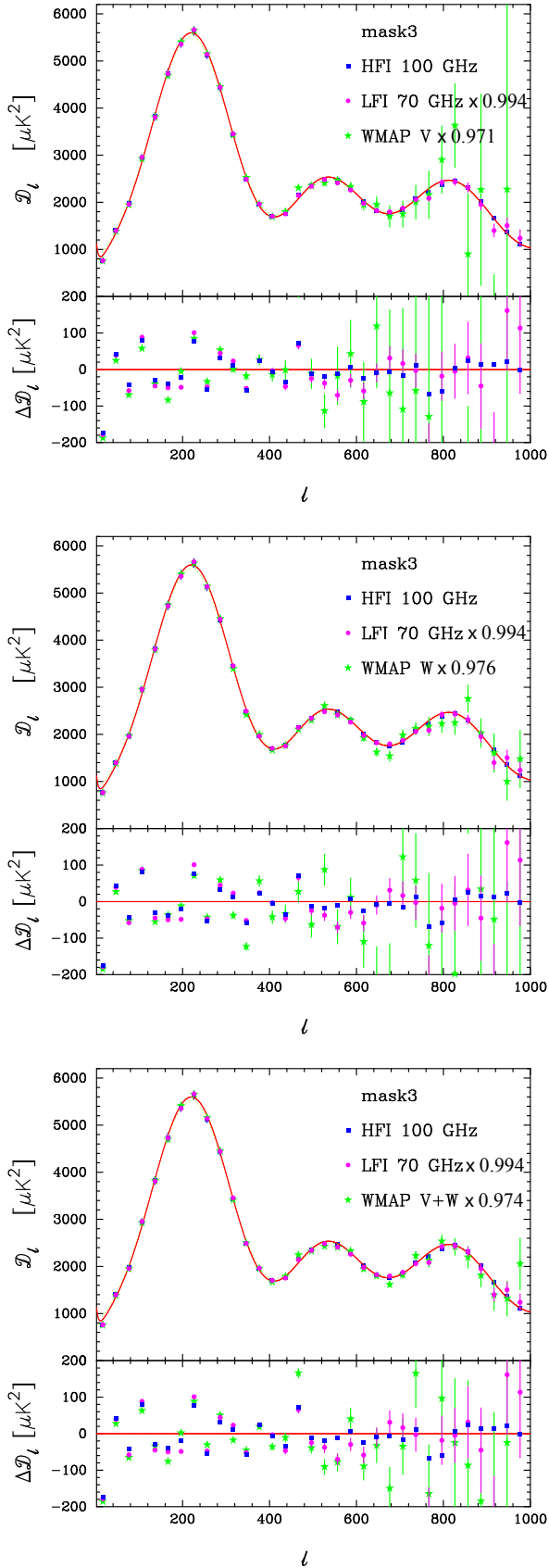
Fig. 23. Foreground-corrected spectra computed using mask G56, with calibration factors c_X from Eq. (3) applied to 70 GHz, *V*, *W*, and *V* + *W*. The solid red lines in the upper panels show the best-fit model CMB spectrum (Planck Collaboration XVI 2014). The lower panels show the residuals with respect to this model. The error bars on the LFI and WMAP points show noise errors only.

between the power spectra of the two experiments therefore have little impact on cosmological parameters.

7. Conclusions

Data consistency in CMB experiments is an important indicator of the validity of the results derived from these data. We have compared calibrated data from different *Planck* channels in three ways: (1) comparison of power spectra calculated on masked, publicly-released maps at 70, 100, and 143 GHz, including corrections for residual unresolved sources; (2) comparison of calibration factors determined to minimize differences between the CMB in the maps; and (3) comparison of power spectra and calibration factors obtained in the likelihood analysis used to determine cosmological parameters. We have emphasized particularly the comparison of 70 GHz and 100 GHz, as these frequencies come from different instruments and are analysed independently, and are near the diffuse foreground minimum. The internal consistency of the *Planck* data is remarkable (relative calibration inconsistencies between CMB channels of only a few tenths of a percent), and is at a level consistent with the uncertainties based on the 2013 solar dipole calibration scheme. In the future, calibration based on the orbital dipole should lead to more accurate absolute calibration.

The estimate of the contribution of the near sidelobes to the HFI beam solid angles in March 2013 implicitly assumed azimuthal symmetry of the near sidelobes. Subsequent analyses of the beam and calibration procedures suggest that this assumption underestimated near-sidelobe power by as much as 0.1%. Corrections for this missing power result in improved agreement between 70 and 100 GHz, measured by ratios of power spectra, at a level of typically 0.3%, well below the levels of uncertainty estimated for LFI and HFI calibration, and therefore having little effect on the cosmological parameters determined from the 2013 data.

Similar analysis applied to WMAP data shows a roughly 2% difference between *Planck* and WMAP over the region of the first acoustic peak. At present, the explanation for this discrepancy with WMAP is not known.

Precision calibration is an ongoing challenge. Future analyses will incorporate the lessons of this study of consistency, further reducing the size of uncertainties and errors on the scientific results from *Planck*.

Appendix A: Difference maps

Figure A.1 shows the frequency maps and difference maps used to calculate the rms values given in Table 1. Frequency maps are half-ring sums. Difference maps are half-ring differences. The maps have been processed as described in Sect. 2 to retain structure between angular scales of 15′ and 8°. Figure 4 gives the corresponding histograms.
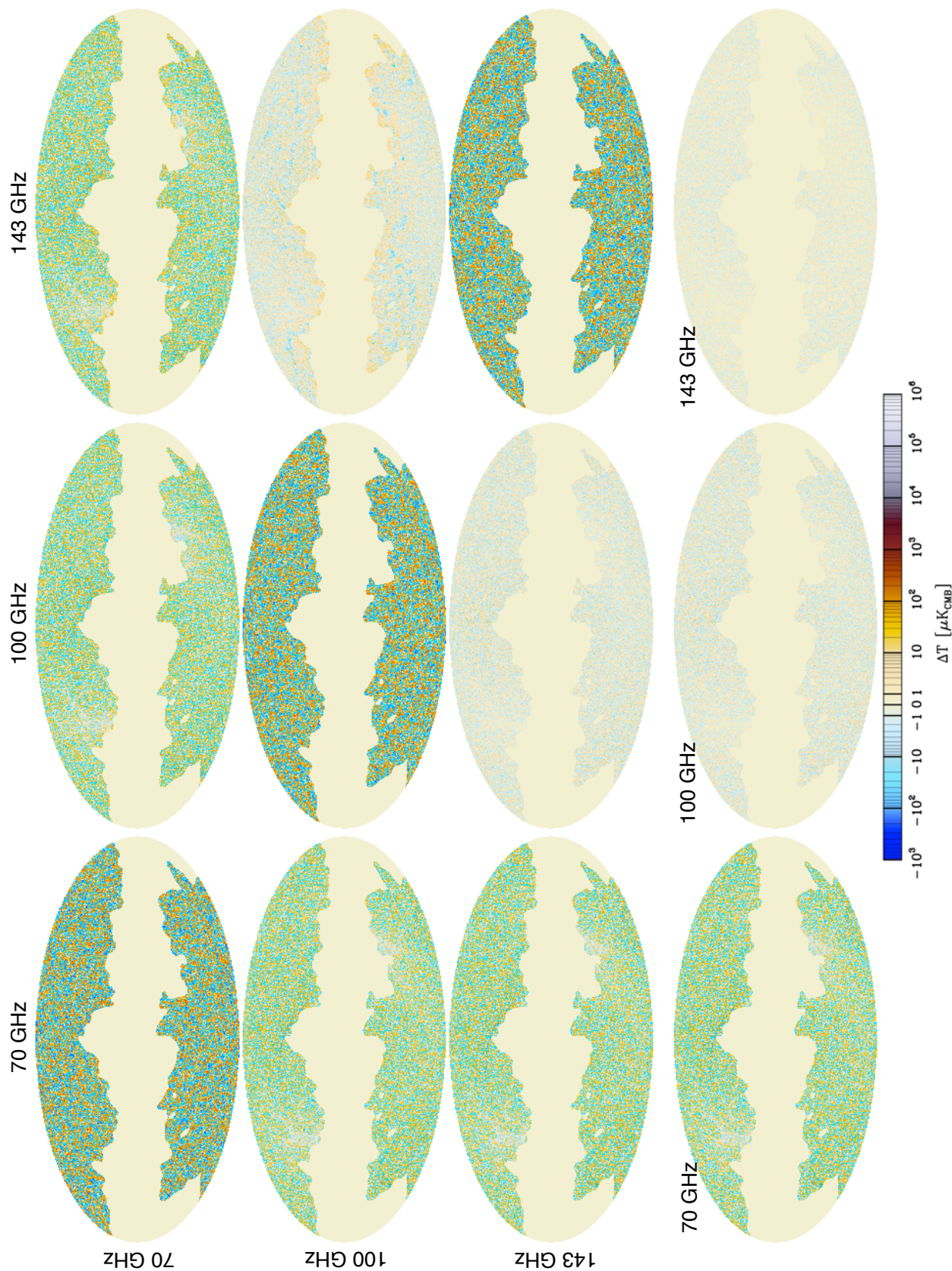
Fig. A.1. Frequency maps and difference maps using the GAL060 mask. Rms values are given in Table 1; histograms are shown in Fig. 4. In the top 3 × 3 group, the frequency maps are on the diagonal. The three frequency difference maps are in the *upper right* block. The noise difference maps are in the *lower left* block. The caption of Fig. 4 describes characteristics of the histograms that can also be seen quite clearly in these maps. The three *upper right* maps are the same as the three in Fig. 3, but with structure on scales larger than 8° removed, as described in the text.

Appendix B: Nominal beam calibration: definitions, approximations, and rescaling factors

In the *Planck* scanning strategy, for each pointing period, the spin axis remains fixed and the output voltage sees a spin-synchronous modulation as the telescope points at direction $\hat{x}$ along a scan circle. The output signal (in arbitrary units) measured by a given *Planck* detector, either LFI or HFI, can be written as

$$V_{\text{out}}(\hat{x}) = G[P * (T_{\text{sky}} + D)](\hat{x}) + M(\hat{p}), \tag{B.1}$$

where P is the angular response ("beam"), normalized to unit solid angle ($\int_{4\pi} P \, d\Omega = 1$), D is the dipole signal (including the solar and orbital terms), T_{sky} is the sky brightness temperature (CMB and foregrounds, i.e., everything *other* than the dipole), and M is a small monopole term assumed to be constant for each pointing period $\hat{p}$. We use the convolution notation $A * P = \int_{4\pi} AP \, d\Omega$.

For each pointing period, the output voltage measures a spin-synchronous modulation dominated by the dipole, which is used to recover a gain calibration factor. The dipole term, $P * D$, is dominant (by two orders of magnitude) once strong foreground regions are masked, so for calibration purposes we have $V_{\text{out}} = G(P * D)$. For each pointing period, calibration is performed by fitting V_{out} to a model of the beam-convolved dipole:

$$\widetilde{G} = \frac{V_{\text{out}}}{(P * D)_{\text{model}}}, \tag{B.2}$$

where $\widetilde{G}$ is the estimated gain, while $G = V_{\text{out}}/(P * D)$ is the true gain. For the 2013 release, we rely on the a priori knowledge of the solar dipole from WMAP (Hinshaw et al. 2009). Relative changes of the gain $G(\hat{p})$ between sky circles contribute to the monopole term $M(\hat{p})$, and are removed by destriping. Assuming an error-free knowledge of the true dipole and of the full beam pattern, then $V_{\text{out}} = (P * D)_{\text{model}}$ and $\widetilde{G} = G$, so one would recover the true value of the gain, preserving the entire power entering the beam. However, full beam convolution was not implemented in the LFI and HFI pipelines for the 2013 release, and we adopted a "nominal beam approximation" approach.

B.1. Nominal beam approximation

We approximate the beam pattern with a "pencil beam", i.e., a normalized delta-function:

$$(P * D)_{\text{model}} = \int_{4\pi} P_{\text{pencil}} D_{\text{model}} d\Omega = P_{\text{pencil}} * D_{\text{model}}. \tag{B.3}$$

Neglecting intrinsic errors in the model dipole ($D_{\text{model}} \approx D$), the estimated gain is

$$\widetilde{G} = G \frac{(P * D)}{(P_{\text{pencil}} * D)}. \tag{B.4}$$

We can write P as the sum of two terms, $P = P_{\text{nominal}} + P_{\text{side}}$, where P_{nominal} represents the contribution of the nominal beam (defined as the portion of the beam defining the window function, see Sect. 4) and P_{side} is the contribution from the (near and far) sidelobes. We have

$$\widetilde{G} = G \frac{(P_{\text{nominal}} * D) + (P_{\text{side}} * D)}{(P_{\text{pencil}} * D)}. \tag{B.5}$$

The convolution of the nominal beam to the dipole is nearly identical to an ideal pencil beam convolution, except that only

a fraction $(1 - f_{\text{sl}})$ of the antenna gain is contained in the nominal beam, so we have

$$P_{\text{nominal}} * D \approx (1 - f_{\text{sl}})P_{\text{pencil}} * D = (1 - f_{\text{sl}})D, \tag{B.6}$$

where f_{sl} is the solid angle fraction of the sidelobes. For the 70, 100, and 143 GHz channels, $f_{\text{sl}} \approx 0.7$, 0.5, and 0.5% (see Sect. 4.1). In this formalism, we assume that the time response of the bolometers has been accurately deconvolved; thus no additional time constant corrections are needed. This approximation is true to high accuracy (<0.2%), since the dipole changes very little within the nominal beam solid angle. Rearranging the terms, we find

$$\widetilde{G} = G(1 - f_{\text{sl}})(1 + \phi_D), \tag{B.7}$$

where $\phi_D \equiv (P_{\text{side}} * D)/(P_{\text{nominal}} * D)$ represents the coupling of the dipole with sidelobes and depends on the detailed structure of the sidelobes and the scanning strategy. Equation (B.7) gives the correction factor that one should apply to recover the proper gain factor if one models the beam as a pencil beam.

B.2. Rescaling factor

To obtain the reconstructed sky signal after calibration, $\widetilde{T}_{\text{sky}}(\hat{x})$, the dipole term needs to be subtracted from the timelines (Eq. (B.1)). Since we are interested in the signal from the sky entering the nominal beam, the coupling of T_{sky} with sidelobes represents a spurious additive signal. So we write the timeline as

$$V_{\text{out}}(\hat{x}) = G(P_{\text{nominal}} * T_{\text{sky}} + P_{\text{side}} * T_{\text{sky}})(\hat{x}) + M(\hat{p}). \tag{B.8}$$

In the ideal case of an error-free, full-convolution model, $\widetilde{G} = G$, one gets

$$\widetilde{T}_{\text{sky}} = \frac{V_{\text{out}}}{\widetilde{G}} = P_{\text{nominal}} * T_{\text{sky}} + P_{\text{side}} * T_{\text{sky}}. \tag{B.9}$$

For angular scales larger than the nominal beam, a relation similar to Eq. (B.6) holds for T_{sky}, i.e., $P_{\text{nominal}} * T_{\text{sky}} \approx (1 - f_{\text{sl}})T_{\text{sky}}$. With this and Eq. (B.9), we obtain

$$T_{\text{sky}} = \widetilde{T}_{\text{sky}} \frac{1 - \phi_{\text{sky}}}{1 - f_{\text{sl}}}, \tag{B.10}$$

where $\phi_{\text{sky}} \equiv (P_{\text{side}} * T_{\text{sky}})/\widetilde{T}_{\text{sky}}$ represents the coupling of the sidelobes with the sky signal (other than the dipole), i.e., the straylight pickup.

As mentioned, however, in the 2013 release both LFI and HFI used the nominal beam approximation. In this case, the estimated gain is given by Eq. (B.7), and we have

$$\widetilde{T}_{\text{sky}} = \frac{V_{\text{out}}}{\widetilde{G}} = \frac{(P_{\text{nominal}} * T_{\text{sky}}) + (P_{\text{side}} * T_{\text{sky}})}{(1 - f_{\text{sl}})(1 + \phi_D)}. \tag{B.11}$$

Solving for the true sky temperature we find

$$T_{\text{sky}} = \widetilde{T}_{\text{sky}} \left[1 - \frac{\phi_{\text{sky}}}{(1 - f_{\text{sl}})} + \phi_D \right] \approx \widetilde{T}_{\text{sky}} \left(1 - \phi_{\text{sky}} + \phi_D \right). \tag{B.12}$$

This expression does not contain the term f_{sl} to first order; however, the (smaller) correction terms ϕ_D and ϕ_{sky} need to be evaluated to derive the proper normalization of the temperature maps and of the power spectra.

In summary, to evaluate the true sky temperature from the estimated one, some correction factors need to be evaluated to

properly account for the beam. These correction terms depend on the model assumptions. For a full convolution model, the rescaling factor is $\eta = (1 - \phi_{sky})(1 - f_{sl})$. For a pencil beam approximation, currently applied by both *Planck* instruments, the rescaling factor is $\eta = (1 - \phi_{sky} + \phi_D)$.

If one were to apply a correction, a rescaling factor η could be directly applied to the temperature map to give a properly calibrated map. Alternatively, the window function should be rescaled by η^{-2}.

B.3. Semi-analytical expression for ϕ_D

A useful expression for ϕ_D can be obtained as follows. The dipole seen through any particular line of sight (LOS) will be proportional to the dot product of the dipole vector with that of the line of sight:

$$D = D_0 \left[\sin \Theta_{LOS} \cos(\Phi_{LOS} - \Phi_D) + \cos \Theta_D \sin \Theta_{LOS} \right], \quad (B.13)$$

where $D_0 = 3.35$ mK, the amplitude of the dipole, Θ_D and Φ_D are the polar and azimuthal angles of the direction of the dipole maximum on the sky[9], and Θ_{LOS} and Φ_{LOS} are the same for the direction of the nominal beam observation. For each ring, choosing a coordinate system for which the z-axis is aligned with the satellite spin axis, and around which both the LOS and the dipole axis will rotate, ensures that the last term in Eq. (B.13) is constant. Since a constant is removed for each stable pointing period (Planck Collaboration VIII 2014), we ignore this and write

$$D = D_0 \sin \Theta_{LOS} \cos(\Phi_{LOS} - \Phi_D). \quad (B.14)$$

Specializing, when the line of sight (LOS) is the nominal beam, the signal seen will be

$$D_{main} = D_0 \sin \Theta_{main} \cos(\Phi_{main} - \Phi_D). \quad (B.15)$$

Similarly, when we observe a point on the sky through a sidelobe, we have

$$D_{sl} = D_0 \sin \Theta_{sl} \cos(\Phi_{main} + \Delta\Phi_{sl} - \Phi_D), \quad (B.16)$$

where $\Delta\Phi_{sl} = \Phi_{sl} - \Phi_{main}$ is the difference in azimuthal angles between the nominal beam and the sidelobe of interest. This yields:

$$\begin{aligned} D_{sl} &= D_0 \sin \Theta_{sl} \cos(\Delta\Phi_{sl}) \cos(\Phi_{main} - \Phi_D) \\ &\quad - D_0 \sin \Theta_{sl} \sin(\Delta\Phi_{sl}) \sin(\Phi_{main} - \Phi_D). \end{aligned} \quad (B.17)$$

Because *Planck* calibrates by "locking in" on, or fitting to, a sinusoidal signal of the form $\cos(\Phi_{main} - \Phi_D)$ (Eq. (B.15)), the second term in Eq. (B.17) is irrelevant, and the far sidelobes will make a contribution to the gain according to

$$\phi_D = \frac{P_{side} * D}{P_{nominal} * D} = \frac{\int_{4\pi} d\Omega \, P(\Theta_{sl}, \Phi_{sl}) \sin \Theta_{sl} \cos(\Delta\Phi_{sl})}{4\pi \sin \Theta_{main}}. \quad (B.18)$$

Integrations over GRASP models of the HFI far sidelobes indicate that $\phi_D \approx f_{FSL}/3$.

---

[9] Note that these angles should include the change to the dipole induced by the satellite motion with respect to the Sun, in addition to that induced by the Sun's motion with respect to the CMB. We have neglected such boosting effects so far – see Planck Collaboration XXVII (2014).
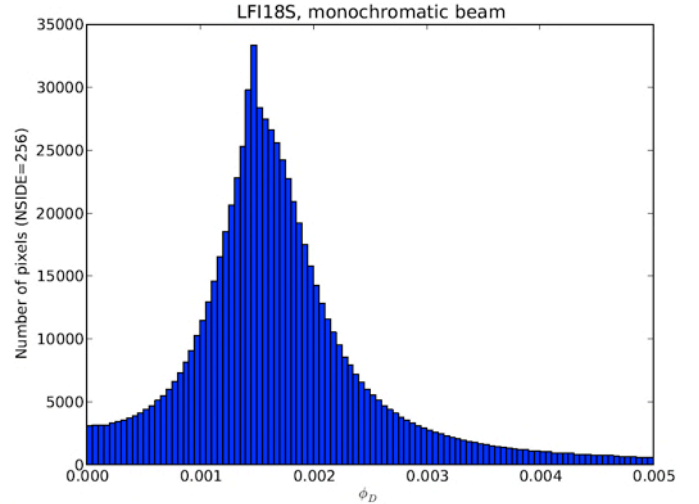
Fig. C.1. ϕ_D for a simulation using a 70 GHz beam.

Appendix C: Assessment of LFI and HFI with respect to beams and calibration

C.1. LFI

C.1.1. Evaluation of ϕ_{sky}

The term ϕ_{sky} turns out to be small, but it is difficult to quantify because it requires a full convolution of a sky model with the full beam, and it is frequency dependent. We have performed a simplified simulation for a 70 GHz channel (LFI18M), and find values for ϕ_{sky} ranging between 0.05% and 0.2% throughout a full survey. More realistic simulations have been produced recently on an LFI 30 GHz channel (LFI27M), for both Survey 1 and Survey 2. We find:

Survey 1, $\langle \phi_{sky} \rangle = 0.05\%$, $0.01\% < \phi_{sky} < 0.23\%$;
Survey 2, $\langle \phi_{sky} \rangle = 0.06\%$, $0.01\% < \phi_{sky} < 1.11\%$.

(Differences between odd and even Surveys are to be expected, given the differences in scanning described in Planck Collaboration I 2014, Sect. 4.1.) These results are consistent with our preliminary findings, and indicate a typical value of $\phi_{sky} \approx 0.05\%$ at all *Planck* frequencies.

C.1.2. Evaluation of ϕ_D

We can estimate ϕ_D by taking average values of the convolutions involved in its definition in Eq. (B.12). The denominator $\langle P_{nominal} * D \rangle = 3.35$ mK is the dipole amplitude. To estimate $\langle P_{side} * D \rangle$, we have computed the convolution of the LFI sidelobes, modelled with GRASP, with the dipole.

Note that ϕ_D contains the effects of both near and far sidelobes; however, it is the dipole modulation through the near sidelobes that contributes most to its value. Destriping removes the contribution from sidelobes nearly aligned with the spacecraft spin axis (such as the "primary spillover," see Planck Collaboration I 2014), which produces a nearly constant offset for each pointing period. After destriping, we find that $\langle P_{side} * D \rangle$ is approximately 3 μK at 70 GHz and 5 μK at 30 GHz, leading to $\langle \phi_D \rangle \approx 0.1\%$ and $\langle \phi_D \rangle \approx 0.15\%$, respectively.

Figure C.1 shows the pixel histogram for a simulation where the value of ϕ_D was computed in every sky direction for an LFI 70 GHz channel. The median value, $\phi_D \approx 0.16\%$, is in good agreement with our first-order estimate.

In conclusion, the correction terms ϕ_D and ϕ_{sky} are of the same order (0.15% and 0.05%, respectively) and tend to cancel each other in Eq. (B.12), resulting in a net effect of $\approx 0.1\%$ on the LFI calibrated map. For the 2013 release, we have not carried out a systematic simulation for all channels; rather we have assumed a conservative residual uncertainty of 0.2% in the LFI calibrated maps due to sidelobe convolution effects (Planck Collaboration V 2014, Table 8). More detailed analysis is planned for the 2014 release.
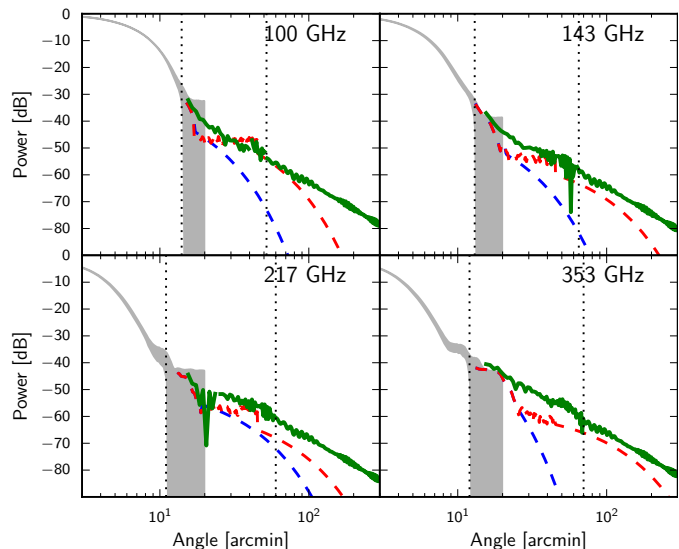
C.2. HFI

The effective beam window function, including the effects of both calibration and map reconstruction, is based on measurements of the scanning beam (Planck Collaboration VII 2014). These are obtained from Mars observations after deconvolution of the time response of the detection chain. The effective beam window function is used to correct the cross-power spectra used in the cosmological analysis. Figure 10 of Planck Collaboration VII (2014) shows this scanning beam, and provides estimates of the near sidelobe contribution to the solid angle between 0.1 and 0.2% at 100 and 143 GHz, respectively. In the subsections below, we estimate the impact of the approximations used in estimating the nominal beam and near sidelobe region (up to 5° from the beam centre) through the use of Saturn and Jupiter observations. We estimate the bias introduced by these approximations, as well as the bias in the calibration factor due to the far sidelobes. As previously stated, we make no attempt to recalibrate the 2013 data release, but only show that the LFI–HFI differences at intermediate multipoles are understood within the present uncertainties.

C.2.1. Nominal beam and near sidelobes

The *nominal beam* for HFI is measured to roughly 15′ with Mars observations. This provides most of the information needed for the high-ℓ analysis used to obtain the 2013 *Planck* cosmological results. Jupiter observations show shoulders extending to 20′ for all channels (see fogire 10 of Planck Collaboration VII 2014). Features in this region are small and difficult to measure. Their integrated contribution, however, is not negligible at the level of a few tenths of a percent. Table 2 and Fig. 10 of Planck Collaboration VII (2014) show estimates of the near sidelobe contribution to the solid angle of between 0.1 and 0.22%.

In addition, pre-launch optical calculations show that at a few FWHM from the beam centre, the HFI beam will have a diffraction pattern from the secondary mirror edges (the pupil of the *Planck* optical system). Figure 14 of Planck Collaboration VII (2014) shows that at 353 GHz there are near sidelobes with a diffraction signature, which have not been accounted for. These features are expected from optical calculations, and they were seen in the pre-launch test campaign. A reanalysis of Saturn and Jupiter data has been carried out for all frequencies, and the near sidelobe wing due to diffraction by the edge of the secondary is seen at least at 143 GHz and higher frequencies. Additionally, the sidelobe profiles of Planck Collaboration VII (2014) led to a removal of the residual time response effects with a weighting that also removed optical near sidelobe signal around 20′.

In order to assess the impact of a more refined accounting of the near sidelobes, we have constructed a new hybrid beam profile that consists of the nominal beam, azimuthally averaged Jupiter observations, and GRASP simulations. The azimuthally averaged Jupiter observations extend to 2°, and include all residual time response and mirror dimpling effects. The astrophysical


Fig. C.2. HFI beam and planet measurement profiles. The grey shaded region shows the 1σ errors in the nominal beam profile used to make the effective beam window function. The dashed blue and red lines are the best-case and worst-case near sidelobe estimates from Jupiter, presented in Fig. 10 of Planck Collaboration VII (2014). The solid green curve is the hybrid beam profile used to derive correction factors here. The vertical dotted lines indicate the radial extent of each portion of the hybrid beam: the nominal beam is at small angles; at intermediate angles Jupiter data are used; and at large angles the scaled GRASP simulation is used.

background is subtracted from each observation, and we fit a baseline and a scaling factor to match the Jupiter profile to the Mars profile at an overlap angle. The GRASP simulations consist of all eight 100 GHz detectors simulated at five frequencies across the band. A 100 GHz full-frequency beam is constructed by weighting the simulations with the map-making weights, detector bandpass, and planet spectral energy distribution. At large angle, the GRASP calculations are dominated by diffraction around the secondary mirror. The diffraction pattern has a similar angular dependence at all HFI frequencies, and its normalization is set by the edge taper of the secondary. We therefore scale the 100 GHz simulations to higher frequencies by fitting to the Jupiter profile. Figure C.2 shows the radial profiles of the hybrid beams, compared with those given in Planck Collaboration VII (2014).

The Saturn-Jupiter combination (Fig. C.2) gives a diffraction pattern similar to that predicted and measured preflight (Tauber et al. 2010). This increases the estimate of the contribution of the near sidelobes to the total solid angle of beam, as given in Fig. 10 of Planck Collaboration VII (2014). However, the dominant contribution to the increase in solid angle at 100 and 143 GHz occurs around 20′, and is due to removing the assumption of azimuthal symmetry and applying no time response correction when computing the radial profile.

This also affects the shape of the effective beam window function, with a decrease similar to that illustrated in the green curve in Fig. 19 of Planck Collaboration VII (2014), although with a larger amplitude and large error bars (Fig. C.3). The effect of these corrections for near-sidelobe power missing in the beams used in the 2013 results is illustrated in Fig. 12. The error in the integral of the beam profile is dominated by the background removal and inter-calibration of the Mars and Jupiter data.
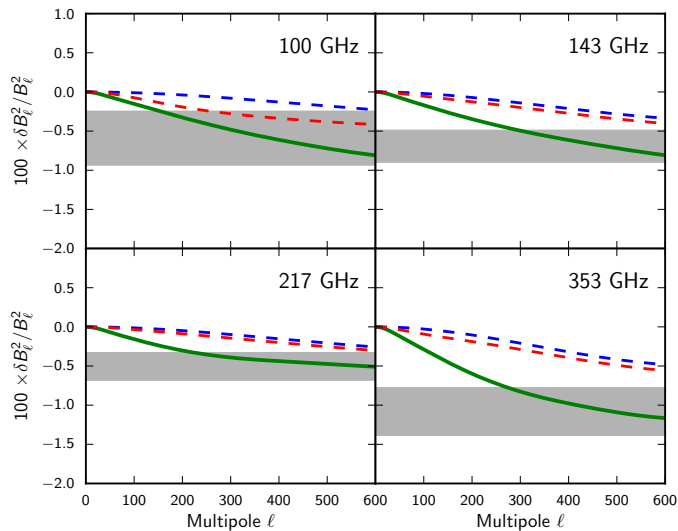
Fig. C.3. Effective beam window function corrections based on the hybrid beam profile. The green curve shows the correction based on the hybrid model presented here. The dashed blue and red lines are the best-case and worst-case near sidelobe estimates from Jupiter, as shown in Fig. 10 of Planck Collaboration VII (2014). The grey shaded region shows the $\pm 1\sigma$ errors in the correction to the solid angle.

C.2.2. Far sidelobes

Estimates from Tauber et al. (2010) put the integrated solid angle of the far sidelobes at roughly 0.3% of the total beam solid angle. While this is small, a significant fraction of this solid angle appears near the satellite spin axis. This means that the signal seen through this part of the sidelobes is not modulated by the satellite rotation, and therefore does not contribute to the calibration. Using calculations such as those in Sect. C.1.2, we estimate the far sidelobe effect on the calibration to be of order one-third the total solid angle for the far sidelobes. For HFI, this constitutes about 0.1% at 100 and 143 GHz.

References

Bennett, C. L., Larson, D., Weiland, J. L., et al. 2013, ApJS, 208, 20
Górski, K. M., Hivon, E., Banday, A. J., et al. 2005, ApJ, 622, 759
Hinshaw, G., Weiland, J. L., Hill, R. S., et al. 2009, ApJS, 180, 225
Hivon, E., Górski, K. M., Netterfield, C. B., et al. 2002, ApJ, 567, 2
Mitra, S., Rocha, G., Górski, K. M., et al. 2011, ApJS, 193, 5
Planck Collaboration I. 2014, A&A, 571, A1
Planck Collaboration II. 2014, A&A, 571, A2
Planck Collaboration III. 2014, A&A, 571, A3
Planck Collaboration IV. 2014, A&A, 571, A4
Planck Collaboration V. 2014, A&A, 571, A5
Planck Collaboration VI. 2014, A&A, 571, A6
Planck Collaboration VII. 2014, A&A, 571, A7
Planck Collaboration VIII. 2014, A&A, 571, A8
Planck Collaboration IX. 2014, A&A, 571, A9
Planck Collaboration X. 2014, A&A, 571, A10
Planck Collaboration XI. 2014, A&A, 571, A11
Planck Collaboration XII. 2014, A&A, 571, A12
Planck Collaboration XIII. 2014, A&A, 571, A13
Planck Collaboration XIV. 2014, A&A, 571, A14
Planck Collaboration XV. 2014, A&A, 571, A15
Planck Collaboration XVI. 2014, A&A, 571, A16
Planck Collaboration XVII. 2014, A&A, 571, A17
Planck Collaboration XVIII. 2014, A&A, 571, A18
Planck Collaboration XIX. 2014, A&A, 571, A19
Planck Collaboration XX. 2014, A&A, 571, A20
Planck Collaboration XXI. 2014, A&A, 571, A21
Planck Collaboration XXII. 2014, A&A, 571, A22
Planck Collaboration XXIII. 2014, A&A, 571, A23
Planck Collaboration XXIV. 2014, A&A, 571, A24
Planck Collaboration XXV. 2014, A&A, 571, A25
Planck Collaboration XXVI. 2014, A&A, 571, A26
Planck Collaboration XXVII. 2014, A&A, 571, A27
Planck Collaboration XXVIII. 2014, A&A, 571, A28
Planck Collaboration XXIX. 2014, A&A, 571, A29
Planck Collaboration XXX. 2014, A&A, 571, A30
Planck Collaboration XXXI. 2014, A&A, 571, A31
Tauber, J. A., Norgaard-Nielsen, H. U., Ade, P. A. R., et al. 2010, A&A, 520, A2

[1] APC, AstroParticule et Cosmologie, Université Paris Diderot, CNRS/IN2P3, CEA/lrfu, Observatoire de Paris, Sorbonne Paris Cité, 10 rue Alice Domon et Léonie Duquet, 75205 Paris Cedex 13, France

[2] Aalto University Metsähovi Radio Observatory and Dept of Radio Science and Engineering, PO Box 13000, 00076 Aalto, Finland

[3] African Institute for Mathematical Sciences, 6-8 Melrose Road, 7945 Muizenberg, Cape Town, South Africa

[4] Agenzia Spaziale Italiana Science Data Center, Via del Politecnico snc, 00133 Roma, Italy

[5] Agenzia Spaziale Italiana, Viale Liegi 26, Roma, Italy

[6] Astrophysics Group, Cavendish Laboratory, University of Cambridge, J J Thomson Avenue, Cambridge CB3 0HE, UK

[7] Astrophysics & Cosmology Research Unit, School of Mathematics, Statistics & Computer Science, University of KwaZulu-Natal, Westville Campus, Private Bag X54001, 4000 Durban, South Africa

[8] CITA, University of Toronto, 60 St. George St., Toronto, ON M5S 3H8, Canada

[9] CNRS, IRAP, 9 Av. Colonel Roche, BP 44346, 31028 Toulouse Cedex 4, France

[10] California Institute of Technology, Pasadena, California, USA

[11] Centre for Theoretical Cosmology, DAMTP, University of Cambridge, Wilberforce Road, Cambridge CB3 0WA, UK

[12] Computational Cosmology Center, Lawrence Berkeley National Laboratory, Berkeley, California, USA

[13] DSM/Irfu/SPP, CEA-Saclay, 91191 Gif-sur-Yvette Cedex, France

[14] DTU Space, National Space Institute, Technical University of Denmark, Elektrovej 327, 2800 Kgs. Lyngby, Denmark

[15] Département de Physique Théorique, Université de Genève, 24 quai E. Ansermet, 1211 Genève 4, Switzerland

[16] Departamento de Física, Universidad de Oviedo, Avda. Calvo Sotelo s/n, 33007 Oviedo, Spain

[17] Department of Astrophysics/IMAPP, Radboud University Nijmegen, PO Box 9010, 6500 GL Nijmegen, The Netherlands

[18] Department of Electrical Engineering and Computer Sciences, University of California, Berkeley, California, USA

[19] Department of Physics & Astronomy, University of British Columbia, 6224 Agricultural Road, Vancouver, British Columbia, Canada

[20] Department of Physics and Astronomy, Dana and David Dornsife College of Letter, Arts and Sciences, University of Southern California, Los Angeles, CA 90089, USA

[21] Department of Physics and Astronomy, University College London, London WC1E 6BT, UK

[22] Department of Physics, Florida State University, Keen Physics Building, 77 Chieftan Way, Tallahassee, Florida, USA

[23] Department of Physics, Gustaf Hällströmin katu 2a, University of Helsinki, 00014 Helsinki, Finland

[24] Department of Physics, Princeton University, Princeton, New Jersey, USA

[25] Department of Physics, University of California, Santa Barbara, California, USA

[26] Department of Physics, University of Illinois at Urbana-Champaign, 1110 West Green Street, Urbana, Illinois, USA

[27] Dipartimento di Fisica e Astronomia G. Galilei, Università degli Studi di Padova, via Marzolo 8, 35131 Padova, Italy

[28] Dipartimento di Fisica e Scienze della Terra, Università di Ferrara, Via Saragat 1, 44122 Ferrara, Italy

[29] Dipartimento di Fisica, Università La Sapienza, P.le A. Moro 2, 00185 Roma, Italy

[30] Dipartimento di Fisica, Università degli Studi di Milano, via Celoria, 16, 20133 Milano, Italy

[31] Dipartimento di Fisica, Università degli Studi di Trieste, via A. Valerio 2, 34127 Trieste, Italy

[32] Dipartimento di Fisica, Università di Roma Tor Vergata, via della Ricerca Scientifica, 1, 00133 Roma, Italy

[33] Discovery Center, Niels Bohr Institute, Blegdamsvej 17, 2100 Copenhagen, Denmark

[34] Dpto. Astrofísica, Universidad de La Laguna (ULL), 38206 La Laguna, Tenerife, Spain

[35] European Space Agency, ESAC, Planck Science Office, Camino bajo del Castillo, s/n, Urbanización Villafranca del Castillo, 28691 Villanueva de la Cañada, Madrid, Spain

[36] European Space Agency, ESTEC, Keplerlaan 1, 2201 AZ Noordwijk, The Netherlands

[37] Finnish Centre for Astronomy with ESO (FINCA), University of Turku, Väisäläntie 20, Piikkiö 21500, Finland

[38] Haverford College Astronomy Department, 370 Lancaster Avenue, Haverford, Pennsylvania, USA

[39] Helsinki Institute of Physics, Gustaf Hällströmin katu 2, University of Helsinki, 00014 Helsinki, Finland

[40] INAF – Osservatorio Astronomico di Padova, Vicolo dell'Osservatorio 5, 35122 Padova, Italy

[41] INAF – Osservatorio Astronomico di Roma, via di Frascati 33, 00040 Monte Porzio Catone, Italy

[42] INAF – Osservatorio Astronomico di Trieste, via G.B. Tiepolo 11, 34143 Trieste, Italy

[43] INAF/IASF Bologna, via Gobetti 101, 40129 Bologna, Italy

[44] INAF/IASF Milano, via E. Bassini 15, 20133 Milano, Italy

[45] INFN, Sezione di Bologna, via Irnerio 46, 40126 Bologna, Italy

[46] INFN, Sezione di Roma 1, Università di Roma Sapienza, P.le Aldo Moro 2, 00185 Roma, Italy

[47] INFN/National Institute for Nuclear Physics, Via Valerio 2, 34127 Trieste, Italy

[48] IPAG: Institut de Planétologie et d'Astrophysique de Grenoble, Université Joseph Fourier, Grenoble 1/CNRS-INSU, UMR 5274, 38041 Grenoble, France

[49] IUCAA, Post Bag 4, Ganeshkhind, Pune University Campus, 411 007 Pune, India

[50] Imperial College London, Astrophysics group, Blackett Laboratory, Prince Consort Road, London, SW7 2AZ, UK

[51] Infrared Processing and Analysis Center, California Institute of Technology, Pasadena, CA 91125, USA

[52] Institut Universitaire de France, 103 bd Saint-Michel, 75005 Paris, France

[53] Institut d'Astrophysique Spatiale, CNRS (UMR 8617) Université Paris-Sud 11, Bâtiment 121, 91405 Orsay, France

[54] Institut d'Astrophysique de Paris, CNRS (UMR 7095), 98bis boulevard Arago, 75014 Paris, France

[55] Institute for Space Sciences, Bucharest-Magurale, Romania

[56] Institute of Astronomy, University of Cambridge, Madingley Road, Cambridge CB3 0HA, UK

[57] Institute of Theoretical Astrophysics, University of Oslo, Blindern, 0315 Oslo, Norway

[58] Instituto Nacional de Astrofísica, Óptica y Electrónica (INAOE), Apartado Postal 51 y 216, 72000 Puebla, México

[59] Instituto de Astrofísica de Canarias, C/Vía Láctea s/n, 38200 La Laguna, Tenerife, Spain

[60] Instituto de Física de Cantabria (CSIC-Universidad de Cantabria), Avda. de los Castros s/n, 39005 Santander, Spain

[61] Jet Propulsion Laboratory, California Institute of Technology, 4800 Oak Grove Drive, Pasadena, California, USA

[62] Jodrell Bank Centre for Astrophysics, Alan Turing Building, School of Physics and Astronomy, The University of Manchester, Oxford Road, Manchester, M13 9PL, UK

[63] Kavli Institute for Cosmology Cambridge, Madingley Road, Cambridge, CB3 0HA, UK

[64] LAL, Université Paris-Sud, CNRS/IN2P3, Orsay, France

[65] LERMA, CNRS, Observatoire de Paris, 61 avenue de l'Observatoire, 75014 Paris, France

[66] Laboratoire AIM, IRFU/Service d'Astrophysique – CEA/DSM – CNRS – Université Paris Diderot, Bât. 709, CEA-Saclay, 91191 Gif-sur-Yvette Cedex, France

[67] Laboratoire Traitement et Communication de l'Information, CNRS (UMR 5141) and Télécom ParisTech, 46 rue Barrault, 75634 Paris Cedex 13, France

[68] Laboratoire de Physique Subatomique et de Cosmologie, Université Joseph Fourier Grenoble I, CNRS/IN2P3, Institut National Polytechnique de Grenoble, 53 rue des Martyrs, 38026 Grenoble Cedex, France

[69] Laboratoire de Physique Théorique, Université Paris-Sud 11 & CNRS, Bâtiment 210, 91405 Orsay, France

[70] Max-Planck-Institut für Astrophysik, Karl-Schwarzschild-Str. 1, 85741 Garching, Germany

[71] McGill Physics, Ernest Rutherford Physics Building, McGill University, 3600 rue University, Montréal, QC, H3A 2T8, Canada

[72] National University of Ireland, Department of Experimental Physics, Maynooth, Co. Kildare, Ireland

[73] Niels Bohr Institute, Blegdamsvej 17, 2100 Copenhagen, Denmark

[74] Observational Cosmology, Mail Stop 367-17, California Institute of Technology, Pasadena, CA, 91125, USA

[75] SB-ITP-LPPC, EPFL, 1015, Lausanne, Switzerland

[76] SISSA, Astrophysics Sector, via Bonomea 265, 34136 Trieste, Italy

[77] School of Physics and Astronomy, Cardiff University, Queens Buildings, The Parade, Cardiff, CF24 3AA, UK

[78] School of Physics and Astronomy, University of Nottingham, Nottingham NG7 2RD, UK

[79] Space Sciences Laboratory, University of California, Berkeley, California, USA

[80] Special Astrophysical Observatory, Russian Academy of Sciences, Nizhnij Arkhyz, Zelenchukskiy region, 369167 Karachai-Cherkessian Republic, Russia

[81] Theory Division, PH-TH, CERN, 1211 Geneva 23, Switzerland

[82] UPMC Univ Paris 06, UMR7095, 98bis boulevard Arago, 75014 Paris, France

[83] Université de Toulouse, UPS-OMP, IRAP, 31028 Toulouse Cedex 4, France

[84] University of Granada, Departamento de Física Teórica y del Cosmos, Facultad de Ciencias, 18071 Granada, Spain

[85] University of Granada, Instituto Carlos I de Física Teórica y Computacional, Granada, Spain

[86] Warsaw University Observatory, Aleje Ujazdowskie 4, 00-478 Warszawa, Poland